

SURFACE MODIFICATION OF TANTALUM VIA ANODIZATION FOR
ORTHOPEDIC APPLICATIONS

A THESIS SUBMITTED TO
THE GRADUATE SCHOOL OF NATURAL AND APPLIED SCIENCES
OF
MIDDLE EAST TECHNICAL UNIVERSITY

BY

ECE USLU

IN PARTIAL FULFILLMENT OF THE REQUIREMENTS
FOR
THE DEGREE OF MASTER OF SCIENCE
IN
METALLURGICAL AND MATERIALS ENGINEERING

JULY 2020

Approval of the thesis:

**SURFACE MODIFICATION OF TANTALUM VIA ANODIZATION FOR
ORTHOPEDIC APPLICATIONS**

submitted by **ECE USLU** in partial fulfillment of the requirements for the degree of
**Master of Science in Metallurgical and Materials Engineering, Middle East
Technical University** by,

Prof. Dr. Halil Kalıpçılar
Dean, Graduate School of **Natural and Applied Sciences**

Prof. Dr. Cemil Hakan Gür
Head of the Department, **Met. and Mat. Eng.**

Assoc. Prof. Dr. Batur Ercan
Supervisor, **Met. and Mat. Eng., METU**

Examining Committee Members:

Prof. Dr. İshak Karakaya
Metallurgical and Materials Eng, METU

Assoc. Prof. Dr. Batur Ercan
Metallurgical and Materials Eng, METU

Prof. Dr. Hüsnü Emrah Ünalın
Metallurgical and Materials Eng, METU

Prof. Dr. Ayşen Tezcaner
Engineering Sciences, METU

Prof. Dr. Fatih Büyükserin
Biomedical Engineering, TOBB ETU

Date: 20.07.2020

I hereby declare that all information in this document has been obtained and presented in accordance with academic rules and ethical conduct. I also declare that, as required by these rules and conduct, I have fully cited and referenced all material and results that are not original to this work.

Name, Last name : Ece Uslu

Signature :

ABSTRACT

SURFACE MODIFICATION OF TANTALUM VIA ANODIZATION FOR ORTHOPEDIC APPLICATIONS

Uslu, Ece
Master of Science, Metallurgical and Materials Engineering
Supervisor : Assoc. Prof. Dr. Batur Ercan

July 2020, 79 pages

Tantalum has excellent corrosion resistance and mechanical properties suitable for orthopedic applications. However, tantalum exhibits bioinert characteristics and cannot promote desired level of osseointegration with juxtaposed bone tissue. To enhance bioactivity of tantalum, nanoscale surface modification via anodization could be a potential approach. In this study, tantalum foils were modified to obtain surface features with different morphologies, *i.e.* nanotubular, nanodimple, nanoporous and nanocoral, via anodization. By controlling anodization parameters including voltage, anodization duration, temperature and electrolyte concentration, surface feature sizes were precisely fine-tuned in the range of 20-140 nm. In this thesis, anodized tantalum samples were characterized to investigate physical and chemical properties of their surfaces, *i.e.* morphology, crystallinity, hydrophobicity, topography and chemistry. The results indicated that anodized tantalum surfaces consisted of Ta₂O₅ and non-stoichiometric tantalum oxide. Upon the anodization, surface area of the tantalum samples increased up to 2 folds, which was accompanied by up to 3.5 folds increase in the nanophase surface roughness. Initial results indicated enhanced fibroblast proliferation and spreading on nanoporous tantalum surfaces *in vitro*. In line with that study, anodized nanotubular, nanodimple and

nanocoral tantalum and non-anodized tantalum surfaces were interacted with bone cells *in vitro*. Biological studies showed that anodized tantalum surfaces significantly enhanced protein adsorption and, at the same time, improved bone cell proliferation and spreading *in vitro* independent of the anodized surface morphology and feature size.

Keywords: Tantalum, anodization, surface morphology, topography, orthopedics

ÖZ

ORTOPEDİK UYGULAMALAR İÇİN TANTAL YÜZEYLERİN ANODİZASYON YÖNTEMİ İLE MODİFİYE EDİLMESİ

Uslu, Ece
Yüksek Lisans, Metalurji ve Malzeme Mühendisliği
Tez Yöneticisi: Doç. Dr. Batur Ercan

Temmuz 2020, 79 sayfa

Tantal metali yüksek korozyon direncine sahip olan malzemelerden biridir ve sahip olduğu mekanik özelliklerden dolayı ortopedi uygulamaları için uygun bir adaydır. Fakat, tantal yüzeyler vücut içerisinde biyoinört özellikler göstermekte olup, kemik dokuya yeterli seviyede entegre olamamaktadır. Nanoboyutlarda yapılacak yüzey modifikasyonu tantal yüzeylerin biyoaktivitesini artırmak için başvurulacak çözümlerden biridir. Bu tez çalışmasında, tantal yüzeyler anodizasyon yöntemi ile modifiye edilerek, yüzeylerde nanotübüler, nanohendek, nanoporoz ve nanomercan morfolojileri elde edilmiştir. Bununla birlikte, anodizasyon parametrelerinde (voltaj, anodizasyon süresi, sıcaklık, elektrolit konsantrasyonu vb.) yapılan değişikliklerle, boyutlar 20 ila 140 nm arasında değiştirilerek, kemiğin topografisi taklit edilmiştir. Anodize yüzeylerin morfoloji, kristallik, hidrofobisite, yüzey topografisi ve kimyası gibi fiziksel ve kimyasal özellikleri karakterize edilmiştir. Elde edilen sonuçlara göre, anodize tantal yüzeylerinin kimyasında Ta₂O₅ ve alt oksitler bulunduğu gözlemlenmiştir. Ayrıca, anodize numunelerin yüzey alanlarında 2 kat, yüzey pürüzlülüğünde ise 3.5 kata kadar artış gözlemlenmiştir. Daha sonra, anodize ve anodize olmayan yüzeyler kemik hücreleri ve fibroblastlar ile etkileştirilmiştir. Başlangıç çalışması olarak, fibroblast hücreleri ile etkileştirilen nanoporoz tantal

yüzeylerin, fibroblast çoğalmasını ve yayılmasını artırdığı gözlemlenmiştir. Bu çalışma doğrultusunda, nanotübüler, nanomercan ve nanohendek yüzeyler kemik hücreleri ile etkileştirilmiş, ve elde edilen anodize yüzeylerin boyuttan bağımsız olarak protein yapışmasını, kemik hücresi çoğalmasını ve yayılmasını artırdığı gözlemlenmiştir.

Anahtar Kelimeler: Tantal, anodizasyon, yüzey morfolojisi, topography, ortopedi

To my beloved parents...

For your endless support and love in my life...

ACKNOWLEDGMENTS

This work was supported by The Scientific Research Council of Turkey (TÜBİTAK), Grant No: 117M187 and National Grant for Priority Topics in Master Programme-2210C.

Firstly, I would like to thank to my advisor Assoc. Prof. Dr. Batur Ercan for his endless support, guidance and encouragement for both my thesis and daily life advices. He always shares his experience and knowledge with me during my Master. I am very grateful that I have learned a lot from him. Whenever I was about giving up, he encouraged me to go on, so I feel very lucky to work with him. It would be impossible to complete my thesis without his support.

I also would like to thank to my labmates, especially to Çağatay Mert Oral and Didem Mimirolu Kılıçoğlu. They always created a peaceful environment and helped me during my experiments. I would like to express my deepest gratitude to my lovely labmate Didem Mimirolu Kılıçoğlu not only for research advices (especially for biological experiments) but also her sincere friendship and endless support.

I am thankful to all members of METU Metallurgical and Materials Engineering Department and METU Center Lab for their helps for my analysis. I would like to express my deepest gratefulness to Center of Excellence in Biomaterials and Tissue Engineering (BIOMATEN) for their helps in biological analysis and financial support for conferences.

Special thanks to my friends Merve Çobanoğlu and Baturalp Goncagül. You always make me laugh over and encourage me endlessly in my career and social life. I am also grateful to Hazal Çağlan and Beste Mete since my high school years. Despite of our current workloads, you are always next to me and supportive for anything. I pretty sure that I need all of you forever in my life. Most importantly, I would like

to express my sincere gratitude and thanks to Çađrı Özdilek for his endless love, support, encouragement and understandings. I am very lucky that I have him in my life.

Last but not least, I am indebted to my parents, Yurdagül Uslu and Fatih Uslu, to my lovely sister Ezgi Uslu İçli for their love, caring, dedication, sacrifices and supports to educate and prepare me for my future. I also appreciate to my cutest cat Rakun, who passed away but is always in my heart.

TABLE OF CONTENTS

ABSTRACT	v
ÖZ.....	vii
ACKNOWLEDGMENTS	x
TABLE OF CONTENTS	xii
LIST OF TABLES	xv
LIST OF FIGURES.....	xvi
LIST OF ABBREVIATIONS.....	xix
CHAPTERS	
1. INTRODUCTION.....	1
2. LITERATURE REVIEW.....	3
2.1 Osteoarthritis	3
2.2 Problems of Currently Used Orthopedic Implant Materials	4
2.3 Reasons of Surface Modification in Nanoscale	6
2.4 Anodization of Tantalum	7
2.5 Anodization for Biomedical Applications.....	10
2.6 Research Objectives	12
3. FABRICATION AND CELLULAR INTERACTIONS OF NANOPOROUS TANTALUM OXIDE	15
3.1 Materials and Methods.....	15
3.1.1 Materials and Reagents.....	15
3.1.2 Sample Preparation	16
3.1.3 Surface Characterization	16

3.1.4	Cell Culture.....	18
3.1.5	Cell Proliferation	18
3.1.6	Cellular Imaging	19
3.1.7	Cell Morphology.....	19
3.1.8	Statistical Analysis.....	20
3.2	Results.....	20
3.3	Discussion.....	28
3.3.1	Fabrication of Nanoporous Tantalum Oxide Surfaces	28
3.3.2	Fibroblast Proliferation on Nanoporous Tantalum Oxide Surfaces.....	30
4.	CONTROLLING THE NANOFEATURE SIZE AND MORPHOLOGY OF ANODIZED TANTALUM OXIDE SURFACES FOR ENHANCED OSTEOBLAST INTERACTIONS	33
4.1	Materials and Methods	33
4.1.1	Sample Preparation.....	33
4.1.2	Surface Characterization.....	34
4.1.3	Cell Culture.....	35
4.1.4	Cellular Proliferation	36
4.1.5	Protein Adsorption.....	36
4.1.6	Cellular Imaging	37
4.1.7	Cellular Morphology	38
4.1.8	Statistical Analysis.....	38
4.2	Results and Discussion	38

4.3	Supporting Information: Controlling the Nanofeature Size and Morphology of Anodized Tantalum Oxide Surfaces for Enhanced Osteoblast Interactions	58
5.	CONCLUSION AND FUTURE WORK.....	61
	REFERENCES.....	65

LIST OF TABLES

TABLES

Table 2.1 Mechanical Properties of Metallic Implant Materials [28].....	6
---	---

LIST OF FIGURES

FIGURES

Figure 2.1. a) Healthy, b) arthritic and c) replaced knee [13].....	3
Figure 2.2. a) Corrosion and b) bone loosening in hip implant [18].....	4
Figure 2.3. Hierarchical structure of the bone [21,26].....	7
Figure 2.4. Schematic view of anodization of tantalum.....	8
Figure 2.5. a) Current time graph obtained during anodization of tantalum [40] and b) formation mechanism of different morphologies during anodization of tantalum [41].....	9
Figure 2.6. a) Nanotubular/nanodimple, b) nanoporous and c) nanocoral morphologies obtained during anodization of tantalum [39,43,44].....	10
Figure 2.7. a) Fluorescence microscopy images of osteoblasts on smooth tantalum surface and nanotubular tantalum, b) MTT absorbance values for cells on smooth and nanotube array surfaces and c) Alkaline phosphatase activity measured for up to 2 weeks of culture on smooth and nanotube arrays [58].....	12
Figure 3.1. SEM micrographs of a) non-porous tantalum and nanoporous tantalum oxide surfaces having b) 25, c) 35, d) 45 and e) 65 nm average pore size. Scale bars are 500 nm. f) Increase in the average pore size of nanoporous tantalum oxide surfaces with increased anodization duration. Values are mean \pm SE, n=3. g) Current-time graph obtained during anodization of tantalum. Bright-field TEM images of h) NPT25 and i) NPT65 samples. Insets show SAED patterns of these samples. Scale bars for h) and i) are 50 nm.....	21
Figure 3.2. a) Sessile drop water contact angles of non-porous Ta and anodized nanoporous Ta oxide surfaces. *p<0.05 compared to other groups, values are mean \pm SE, n=3. N ₂ gas absorption-desorption hysteresis and pore size distribution of b) NPT25 and c) NPT65 samples.....	23
Figure 3.3. High resolution XPS spectra of a) non-porous tantalum, b) and c) NPT25 and d) and e) NPT65 samples showing a), b) and d) Ta4f and c) and e) O1s peaks.....	24

Figure 3.4. AFM micrographs and line scan profiles of a) non-porous, b) NPT25 and c) NPT65 samples. d) Nanophase and microphase roughness values of non-porous, NPT25 and NPT65 samples. * $p < 0.05$ compared to all others, values are mean \pm SE, $n=3$. Scale bars for AFM micrographs are 400 nm.....26

Figure 3.5. a) Fibroblast density on tantalum samples up to 5 days *in vitro*. Data are mean \pm SE, * $p < 0.05$ compared to all other samples. Actin (green) and nuclei (blue) stained images of fibroblasts cultured on b) non-porous, c) NPT25 and d) NPT65 samples. Scale bars are 50 μm . SE images of fibroblasts cultured on e) non-porous, f) NPT25 and g) NPT65 samples. Scale bars are 10 μm . Higher magnification SEM images of fibroblasts cultured on h) non-porous, i) NPT25 and j) NPT65 samples were given. Scale bars are 5 μm for h), 1 μm for i) and j).....27

Figure 4.1. SEM micrographs of a) non-anodized, b) NT-min, c) NT-max, d) NC-min, e) NC-max, f) ND-min and g) ND-max samples. Insets for NT-min and NT-max show the bottom views of the nanotubular features. Scale bars are 500 nm.....40

Figure 4.2. Graphs indicate a) nanotubular feature size vs. voltage, b) nanotubular oxide layer thickness vs. voltage, c) nanocoral pore size vs. anodization time, d) nanodimple feature size vs. voltage for 30 min anodization. Values are mean \pm SEM, $n=3$42

Figure 4.3. Current vs. time graphs for the anodized tantalum samples.....45

Figure 4.4. Bright-field TEM micrographs of oxide layers obtained from a) NT-min, b) NT-max, c) NC-min and d) NC-max surfaces. Insets indicate SAED patterns.....46

Figure 4.5. High resolution XPS spectra of Ta 4f peaks for a) non-anodized, b) NT-min, c) NT-max, d) NC-min, e) NC-max, f) ND-min and g) ND-max samples.....48

Figure 4.6. Sessile drop water contact angles of non-anodized and anodized tantalum samples. Values are mean \pm SEM, $n=3$ and * $p < 0.05$ compared to all other samples.....49

Figure 4.7. AFM micrographs of a) non-anodized, b) NT-min, c) NT-max, d) NC-min, e) NC-max, f) ND-min and g) ND-max samples. h) Values for the nanophase surface roughness and surface areas of the samples. * $p < 0.01$ compared to all other samples and # $p < 0.01$ compared to non-anodized sample. Scale bars are 400 nm.....51

Figure 4.8. a) 4 h protein adsorption and b) 5 day osteoblast proliferation on anodized and non-anodized tantalum samples. Data are mean \pm SEM, n=3, *p< 0.01 compared to all other samples and #p<0.01 compared to non-anodized tantalum.....54

Figure 4.9. Nucleus (blue), actin fiber (red) and vinculin (green) stained osteoblasts at 3rd day of cultured on non-anodized and anodized tantalum samples. The column on the far right shows the merged images. Scale bars are 20 μ m.....56

Figure 4.10. SEM micrographs of osteoblasts cultured on non-anodized and anodized tantalum samples at low and high magnification.....57

Figure 4.11. Graphs indicate nanodimple feature size vs. voltage for a) 10 min and b) 20 min anodization. Values are mean \pm SEM, n=3.....58

Figure 4.12. a) NT-max samples have free standing nanotubular oxide layer. b) and c) Nanotubular features were not distributed uniformly across the NT-max samples and yellow boxes highlight the regions where delamination occurred.....58

Figure 4.13. Cross-sectional view of an NC sample. Scale bar is 1 μ m.....59

Figure 4.14. Delaminated surface oxide layer of the NC-max samples during cell culture.....59

LIST OF ABBREVIATIONS

ABBREVIATIONS

NTP25	Nanoporous Tantalum having 25 nm Feature Size
NPT35	Nanoporous Tantalum having 35 nm Feature Size
NPT45	Nanoporous Tantalum having 45 nm Feature Size
NPT65	Nanoporous Tantalum having 65 nm Feature Size
NT-min	Nanotubular Tantalum having Minimum Diameter
NT-max	Nanotubular Tantalum having Maximum Diameter
NC-min	Nanocoral Tantalum having Minimum Diameter
NC-max	Nanocoral Tantalum having Maximum Diameter
ND-min	Nanodimple Tantalum having Minimum Diameter
ND-max	Nanodimple Tantalum having Minimum Diameter

CHAPTER 1

INTRODUCTION

Bone is the main part of our skeletal system and provide us mobility. Like other organs and tissues, it may weaken, get damaged or even fracture due to aging, accidents or diseases. To fix, augment and replace damaged bone, orthopedic implants are typically used [1]. Due to increased elderly population and chronic orthopedic diseases such as osteoarthritis, demand for orthopedic implants is increasing steadily worldwide. According to statistical projections, the number of patients who required orthopedic implant was 158 million in 2017, and it will increase 50% by 2040 [2]. However, the lifetime of currently used orthopedic implants is still 15-20 years and it cannot satisfy the needs of patients, especially the younger ones [3]. In fact, younger patients may require more than one orthopedic implant during their lifetimes, and this necessitates revision surgeries, which are riskier and more expensive than the primary surgery [4]. Therefore, better orthopedic implants with increased longevity is required.

Tantalum is a candidate material to improve the longevity of currently-used orthopedic implants due to its remarkable mechanical and chemical properties. In oxygen environment, tantalum forms a stable oxide layer on its surface. This layer prevents ion release from tantalum surfaces and enhances its corrosion resistance [5–7]. In addition, tantalum is considered as biocompatible and porous tantalum has been used in orthopedic applications over 20 years [8]. In spite of these advantages, tantalum still exhibits bioinert properties and cannot provide ideal biological interactions with bone tissue [9]. To overcome this problem, surface modification in the nanoscale can be a remedy [1,10]. Among various surface modification techniques, anodization process, which is an electrochemical surface modification technique, can be used due to its versatility, simplicity and low cost [11,12]. With

anodization process, it is easy to obtain different morphologies on material surfaces and surface feature sizes can be controlled readily.

Although there are promising findings for the use of nanotubular tantalum surfaces in orthopedic applications, a thorough study investigating the anodization parameters to control nanophase surface morphology and feature size, along with assessing the interaction of anodized surfaces with bone cells is missing in the literature. In this study, oxide-based surface features having four distinct morphologies, namely nanotubular, nanodimple, nanocoral and nanoporous having feature sizes specifically tailored between 20 to 140 nm were fabricated via anodization onto tantalum surfaces. Afterwards, as a preliminary study, fibroblasts were interacted with nanoporous tantalum surfaces, followed by a more thorough assessment of human osteoblast (bone cell) interactions with nanotubular, nanocoral and nanodimple surfaces to investigate the influence of anodized tantalum oxide surface morphology and feature size on cellular functions.

CHAPTER 2

LITERATURE REVIEW

2.1 Osteoarthritis

Osteoarthritis, the inflammation of joints due to degenerated cartilage tissue, is the most common joint disease. It limits the mobility of the patients and, in severe cases, necessitates the degenerated tissues to be replaced with an artificial orthopedic implant. Considering the surging geriatric population and the increased demand to use orthopedic implants to younger patients, 15 to 20 year average lifetime of currently-used implants fail to satisfy the clinical needs [3]. In fact, in the USA alone, the demand for primary total hip arthroplasty is anticipated to increase up to 174% by 2030, while the number of revision surgeries will double by 2026 [12]. Specifically, young and active patients require at least one revision surgery, which is riskier than the primary one with a decreased chance for success [4]. Clearly, better orthopedic implants with increased longevity are required.



Figure 2.1. (a) Healthy, (b) arthritic and (c) replaced knee [13]

2.2 Problems of Currently Used Orthopedic Implant Materials

There are several reasons for failure of currently-used orthopedic implants. These include, but not limited to, loosening, inflammation, wear debris formation, fatigue, adverse body response etc. [14]. Among the list of potential orthopedic implant failure mechanisms, loosening and inflammation due to corrosion products are among the most crucial reasons causing up to 40% of revision surgeries [15]. Corrosion, in general, is an electron transfer process taking place on the surface of metals. Since conditions in the implantation site are harsh and very corrosive (*i.e.* low pH) undesirable ions may get released from the orthopedic implant surfaces [16]. In addition to unwanted ion release, corrosion may also weaken mechanical properties. As a result, these released ions may result in inflammation and at the same time, implant cannot bear the load properly due to reduced mechanical properties. Osseointegration is the key factor that provide structural and functional integrity of the implant material with bone tissue [17]. Without proper osseointegration, implant loosening is inevitable, and this eventually results in failure of orthopedic implants.



Figure 2.2 a) Corrosion and b) bone loosening in hip implant [18]

Currently-used metals to fabricate orthopedic implants are stainless steel, CoCrMo, titanium and its alloys. Despite their common use in orthopedic applications, these

materials have various disadvantages. For example, stainless steel contains a certain amount of nickel (Ni) and as a consequence of corrosion processes, Ni ions get released from the stainless-steel surfaces. Since Ni ions are toxic and allergenic, unwanted release of Ni ions may cause adverse body response [19]. Similarly, CoCrMo alloys also contain Ni and chromium (Cr) and corrosion products of this alloy also exhibit toxic and allergenic characteristics. Therefore, both stainless steel and CoCrMo alloys are not suitable for use in orthopedic applications despite having remarkable mechanical properties [20]. Titanium and its alloys (especially Ti6Al4V) are the most commonly used materials in orthopedics due to their mechanical and chemical properties suitable for orthopedic applications, along with their biocompatible nature. However, commercially pure Ti shows low frictional characteristics leading to wear debris formation and Ti6Al4V alloy contains both aluminum (Al) and vanadium (V) which are considered cytotoxic elements [21]. Therefore, researchers are trying to find different candidate materials for orthopedic applications.

Having remarkable mechanical and chemical properties, tantalum is one of the candidate materials to improve the lifetime of currently-used orthopedic implants. It is a transition metal which has density of 16.69 g/cm^3 and melting temperature of 3017°C . It exists in two different crystal structures which are body centered cubic (α -Ta) and tetragonal (β -Ta) [22]. Ta forms a naturally existing oxide layer Ta_2O_5 under ambient conditions, having two orthorhombic polymorphs which are low temperature (β - Ta_2O_5) and high temperature form (α - Ta_2O_5) [23]. This oxide layer forms on tantalum surfaces, and similar to Ti, provides an outstanding corrosion and abrasion resistance. In addition, upon the implantation of tantalum based implants into the body, the surface oxide layer prevents ion release from tantalum surfaces into the surrounding tissues [19,24,25]. Besides, tantalum is considered biocompatible and its porous form has been used in orthopedic applications for over 20 years [26]. Despite the aforementioned advantages tantalum has to offer, it still exhibits bioinert properties and fails to provide the desired level of biological interaction with juxtaposed tissue. In fact, the bioinert nature of tantalum was

associated with delayed bone ingrowth and implant-bone tissue bonding, which eventually resulted in implant loosening [27]. To enhance the bioactivity of tantalum surfaces for successful osseointegration, surface modification in the nanoscale can be a beneficial approach [1,6].

Table 2.1 Mechanical properties of metallic implant materials [28]

Material	E (GPa)	σ_{yield} (MPa)	σ_{ult} (MPa)	% elong
Fe-based	200–205	170–690	540–1000	12–40
Co-based	220–230	450–1500	655–1900	5–30
CP Ti	100–115	170–480	240–550	15–24
Ti-based	100–110	585–1050	690–1150	10–15
Ta	188	140–345	205–480	1–30
Ni-Ti (Ms)	28–41	70–140	895	~9

2.3 Reasons of Surface Modification in Nanoscale

Bone has a hierarchical structure showing different levels of order starting from the nanometer to micrometer level [1]. For example, inorganic matrix of bone consists of apatite crystals which are 20-40 nm in length, while type I collagen, the main protein component in the organic phase of bone, has a width of about 0.5 nm [29,30]. Therefore, bone is considered as a nanostructured material and surface modification of orthopedic implants in the nanoscale mimics the bone topography [31]. In addition, nanostructured materials have a higher surface area to volume ratio compared to their conventional counterparts. Upon the nanoscale modification the implant surfaces, surface properties, including surface chemistry, topography, energy, and etc., would be altered. Implants made of nanostructured surfaces promote altered protein adsorption, which can be engineered to support cellular interactions [32]. As a matter of fact, nanofeatured surfaces were already shown to enhance bone synthesis *in vitro* and *in vivo* [33]. For instance, An *et al.* observed that bone cell (osteoblast) adhesion and proliferation on nanolamellar tantalum fabricated via equal channel angular pressing was higher compared to conventional tantalum having micrometer sized grains [34]. Also, nanograined tantalum surfaces enhanced

osteoblast adhesion, proliferation, spreading and mineralization compared to conventional tantalum. These surfaces also upregulated the expression of osteogenic genes, including ALP, Runx2, osteocalcin, osteopontin, osterix and collagen-I [35].

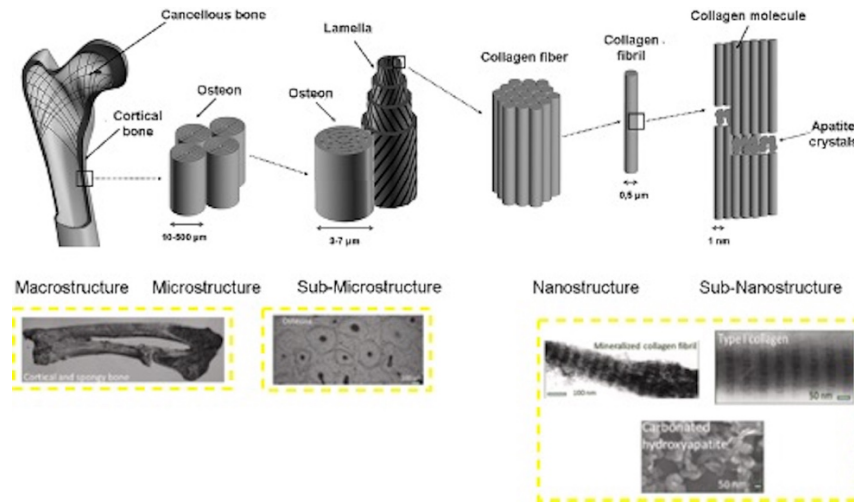


Figure 2.3. Hierarchical structure of the bone [21,36]

2.4 Anodization of Tantalum

Among various surface modification techniques, anodic oxidation (anodization) was studied in the last decade due to its ability to fabricate nanofeatures on metallic surfaces [10,11]. Briefly, anodization is an electrochemical process to grow the naturally occurring oxide layer on valve metals (Ti, Ta, Al, V, Nb, Zr, and etc.). In the anodization process, metal to be anodized (in this case tantalum) is used as an anode and cathode is typically an inert metal (*i.e.* platinum). Via the application of a potential difference between the electrodes, oxygen ions generated at the electrolyte/anode interface move under the action of the electrical field, migrate within the metal attached to the anode and form an oxide surface layer [37]. The control of electrochemical parameters, *i.e.* anodization duration, potential, electrolyte concentration, temperature, pH, and etc., alter oxide layer properties and allow the fabrication of nanofeatured surface morphologies (*i.e.* nanotubes and nanodimples) [19].

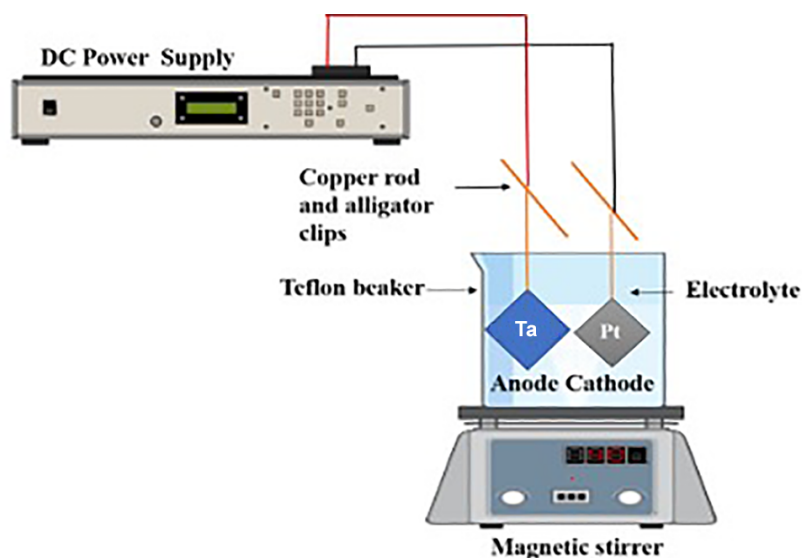
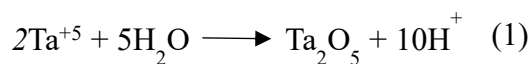


Figure 2.4. Schematic view for anodization of tantalum

In the case of tantalum anodization, once potential is applied across the electrochemical cell, oxidation reaction occurs instantaneously according to reaction (1). Specifically, Ta^{+5} ions migrating towards the electrolyte encounter O^{2-} ions, which are present in the aqueous electrolyte, migrating towards anode. They form compact tantalum oxide layer. When compact oxide layer forms, due to its insulating properties, current density across the system decreases exponentially (Figure 2.5a Region I) [38].



When fluorinated electrolytes are used during anodization, fluoride ions present in the electrolyte start to dissolve compact oxide layer according to reaction (2) and form a fluoride-rich complex at the metal/metal oxide interface. Due to etching effect of fluoride ions, small pits form on the tantalum oxide layer at the beginning. These small pits transform into pores or tubes depending on the fluoride concentration in the electrolyte and current density in the system starts to increase again (Figure 2.5a

Region II). At the same time, number and thickness of these features increases until current density reaches a peak point. Finally, due to the limited diffusion of ions across the oxide layer, current density decreases again (Figure 2.5a Region III), while an equilibrium between oxide formation and oxide dissolution is obtained [38,39].

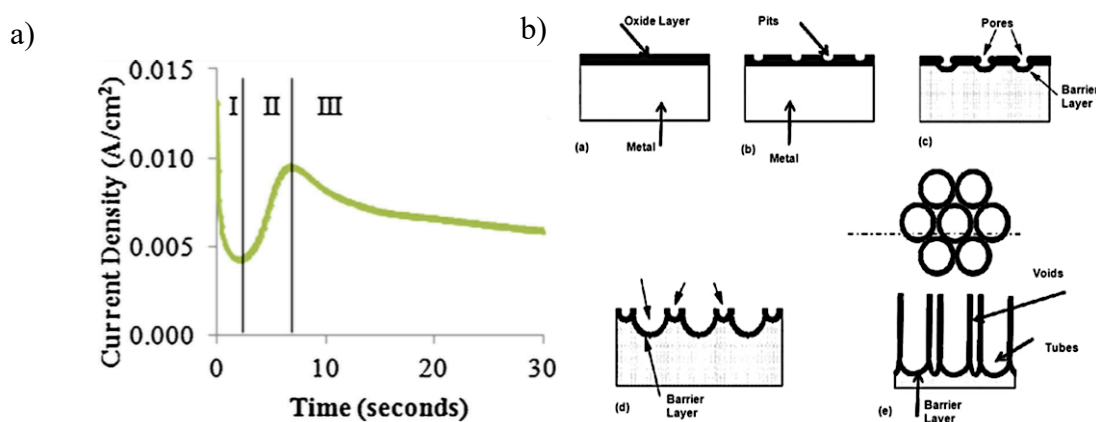


Figure 2.5 a) Current-time graph obtained during anodization of tantalum [40] and b) formation mechanism of different morphologies during anodization of tantalum [41].

There are several studies in the literature investigating anodization of tantalum. For instance, Horwood *et al.* obtained nanotubular tantalum oxide features up to 1 μm in length using H_2SO_4 and HF containing electrolyte where low HF concentration was observed to be an important parameter to obtain thin oxide films. They also observed that nanotube length was proportional to the anodization duration in a linear fashion [40]. El-Sayed *et al.* obtained nanotubular tantalum oxide features under 14.5V potential using 16.4 M H_2SO_4 + 2.9 M HF electrolyte. It was shown that slow increase in the current density led to the formation of unstable nanotubes detached from the surfaces to form dimpled surface morphology, while continuous decrease in the current density led to the formation of stable nanotubes [39]. Nanoporous

tantalum oxide surfaces having 35-65 nm feature size were fabricated using 1 M H_2SO_4 + 3.3 wt% NH_4F solution at 20V potential. The anodized nanoporous tantalum oxide surfaces consisted of multiple porous oxide layers forming on top of each other and the hydrophilicity and roughness of samples were shown to increase after the anodization process [42].

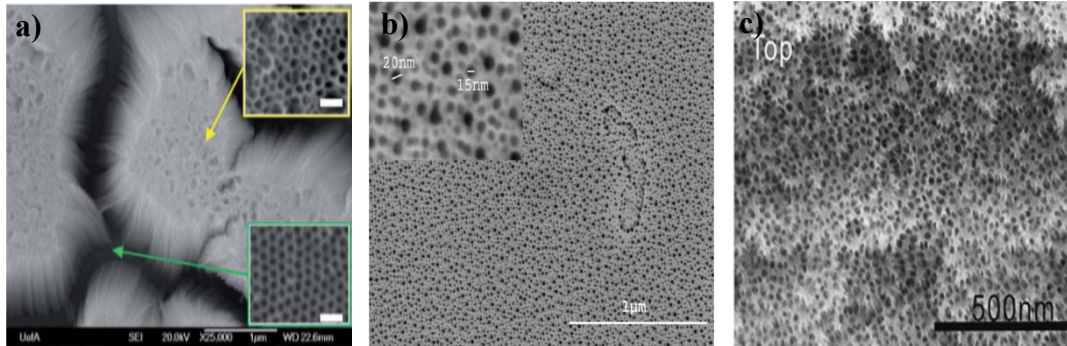


Figure 2.6. a) Nanotubular/nanodimple, b) nanoporous and c) nanocoral morphologies obtained during anodization of tantalum [39,43,44].

2.5 Anodization for Biomedical Applications

In the last decade, nanofeatured oxide surfaces having different chemistries, *i.e.* aluminum oxide and titanium oxide, fabricated via anodization were investigated in detail for their use in biomaterial applications [45–49]. For instance, anodized nanoporous aluminum oxide surfaces were shown to enhance fibroblast, neuronal-like cell and osteoblast adhesion compared to conventional aluminum surfaces [50–52]. They also increased total protein content and extracellular matrix synthesis of osteoblasts, as well as alkaline phosphate (ALP) activity and osteocalcin expression of mesenchymal stem cells *in vitro* [53,54]. Qadir *et.al.* showed that anodized nanotubular features on Ti35Zr28Nb alloy promoted higher Saos-2 adhesion and proliferation compared to surfaces lacking nanofeatures [55]. It was also observed that anodized titanium improved tissue ingrowth and led to improved osseointegration compared to non-anodized Ti in rabbit and pig models *in vivo* [56,57]. Although there is plenty of literature on the biological properties of different

metallic surfaces upon their anodization, research focusing on the cellular interactions of anodized nanofeatured tantalum surfaces and their use in orthopedic applications is very limited. *Wang et al.* observed that nanotubular tantalum oxide surfaces having 20 nm feature size enhanced mesenchymal stem cell adhesion, proliferation and upregulated the expression of ALP, collagen-I and osteocalcin genes compared to conventional tantalum surfaces [9]. Nanotubular tantalum oxide surfaces were also shown to promote cellular viability, ALP activity and calcium deposition of osteoblasts compared to smooth tantalum *in vitro* [58]. Having this said, the effect of nanotubular diameter was also found to influence biological properties. For instance, *Ma et. al.* observed that the adhesion, proliferation and differentiation of mouse bone cells into osteocytes increased upon the decrease in nanotubular tantalum diameter from 126 to 56 nm [24]. A similar trend was also observed for nanoporous tantalum oxides where surfaces having 25 nm pore size enhanced fibroblast adhesion and proliferation compared to the ones having 65 nm pore size and non-porous tantalum [59]. The observed changes in biological properties with changes in anodized surface feature size were not specific to tantalum; anodized nanotubular titanium and Ti6Al4V alloys also expressed size dependent changes in cellular functions. For instance, *Oh et. al.* correlated decrease in anodized nanotubular titanium feature size with an increase in mesenchymal stem cell surface density, while an increase in the nanotube feature size up-regulated ALP, osteocalcin and osteopontin gene expressions [60].

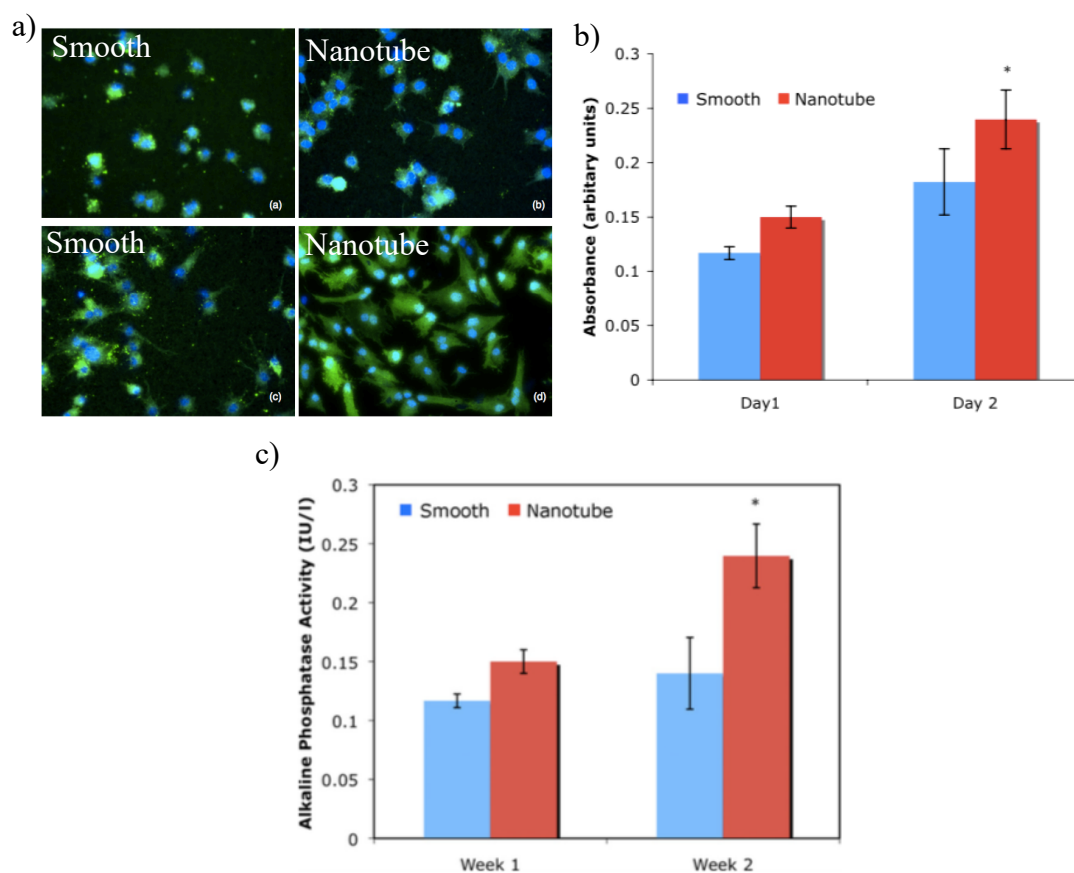


Figure 2.7. a) Fluorescence microscopy images of osteoblasts on smooth tantalum surface and nanotubular tantalum, b) MTT absorbance values for cells on smooth and nanotube array surfaces and c) alkaline phosphatase activity measured for up to 2 weeks of culture on smooth and nanotube arrays [58].

2.6 Research Objectives

Although there are different studies in literature focusing on the anodization of tantalum, there was very limited research investigating the anodized tantalum surfaces for biomedical applications. In this thesis, our research objectives are to:

- obtain four different surface morphologies (nanoporous, nanotubular, nanocoral and nanodimple) on tantalum via anodization,
- precisely control feature sizes between 20 to 140 nm,
- characterize physical and chemical properties of the nanofeatured surfaces,

- investigate biological interactions using fibroblasts and osteoblasts on featured tantalum surfaces.

CHAPTER 3

FABRICATION AND CELLULAR INTERACTIONS OF NANOPOROUS TANTALUM OXIDE

In this study, nanoporous tantalum oxide surfaces having different pore sizes were fabricated via altering the anodization duration. The effect of nanoporous tantalum oxide surface morphology, topography, chemistry and hydrophobicity on the proliferation of fibroblasts was examined for the first time in literature. Results indicated that anodized nanoporous tantalum surfaces enhanced proliferation of fibroblast cells, and thus we propose anodization as a promising surface modification technique to increase cellular interactions with tantalum for tissue engineering applications.

3.1 Materials and Methods

3.1.1.1 Materials and Reagents

Tantalum foils (0.127 mm thick, 99.95% purity) were purchased from Alfa Aesar (Haverhill, Massachusetts). 3-(4,5-dimethyl-2-thiazolyl)-2,5-diphenyl-2-H-tetrazolium bromide (MTT) powder was purchased from Glentham Life Sciences (Wiltshire, United Kingdom). DAPI and Alexa Fluor 488 Phalloidine dyes were purchased from Life Technologies (Carlsbad, California) and Invitrogen (Carlsbad, California), respectively. The rest of the chemicals used in this study were purchased either from Sigma-Aldrich (St. Louis, Missouri) or Merck (Burlington, Massachusetts). The chemicals used in these experiments were analytical grade and no further purification was applied. Aqueous solutions were prepared using ultrapure

water obtained from Millipore Milli-Q purification system (Burlington, Massachusetts).

3.1.2 Sample Preparation

1 cm x 1 cm tantalum samples were successively sonicated in acetone, ethanol and distilled water for 15 min and dried at room temperature. The cleaned samples were anodized using 9:1 (v/v) H₂SO₄ (95-97%):HF (38-40%) aqueous solution under magnetic stirring. A two-electrode electrochemical cell configuration was used where platinum mesh (Thermo Fisher Scientific, Lancashire, UK) was the cathode and tantalum was the anode. The distance between the tantalum anode and the platinum cathode was set to 4 cm and the electrodes were connected to a DC power supply (Genesys 300V/5, TDK Lambda, Achern, Germany) using copper wires. An anodization potential of 30 V was applied between the electrodes. Anodization duration was altered from 5 to 20 min to control tantalum surface properties. Once anodization was completed, samples were rinsed with ultrapure water and placed in air to dry. All anodization experiments were carried out at room temperature.

3.1.3 Surface Characterization

Surface morphology of the samples were characterized with scanning electron microscope (SEM, FEI, Nova Nano 430, Brno, Czech Republic) at 20 kV accelerating voltage using secondary electrons. Prior to SEM analysis, anodized samples were coated with a thin layer of Au-Pd using Quorum SC7640 high resolution sputter coater (Lewes, United Kingdom) to prevent charge build-up. Dimensional characterization of the surface features was completed using ImageJ 1.51 software (National Institute of Health, Bethesda, Maryland). Dimensions for 90 different surface features on each sample were measured and the measurements were repeated in triplicates. To examine the internal structure and crystallinity of the anodized oxide layer, transmission electron microscopy (TEM; JEM 2100F, JEOL,

Tokyo, Japan) was used. For TEM analysis, oxide layers were mechanically removed from the underlying tantalum and suspended in ethanol solution. Afterwards, samples were transferred onto holey carbon coated copper grids and dried in air for 10 min. TEM characterization was completed in bright-field, high resolution (HR) and selected area electron diffraction (SAED) modes using 200 kV accelerating voltage. Hydrophobicity of the samples were characterized with sessile drop water contact technique using a goniometer (EasyDrop, KRÜSS GmbH, Hamburg, Germany). 3 μ L ultrapure water was dropped onto each sample and surface contact angles were measured. Measurements were repeated in triplicates for each sample. Micro scale roughness values of the samples were measured using a profilometer with a scan rate of 2.54 mm/s (Mitutoyo SJ 400, Kanagawa, Japan) across a length of 8 mm. Nanoscale roughness measurements were completed using atomic force microscopy (Veeco, Multimode V, Santa Barbara, California). Topographical images of the samples were captured using the tapping mode with a silicon tip having a radius of 10 nm. A scan rate of 1 Hz was used to characterize 1 μ m x 1 μ m fields on each sample. AFM images were processed using Image Plus (Peseux, Switzerland) software. Root-mean square roughness and surface area values were reported for quantitative analysis of the surface topography. Surface chemistries of the samples were examined using X-ray photo electron spectroscopy (PHI, 5000 Versa Probe, Minnesota, USA). Monochromatic Al K_{α} X-ray source was used with an approximate vacuum pressure of 7 Pa for the analysis. Scans for Ta 4*f*, O 1*s* and C 1*s* orbitals were collected from a spot diameter of 50 μ m. C 1*s* peak at 284.5 eV was used as a reference to correct electrostatic charging of the samples. XPS Peak41 software was used to deconvolute Ta 4*f*_{7/2}, Ta 4*f*_{5/2} and O 1*s* peaks. Pore size distribution of anodized samples was completed by N₂ gas absorption technique using Autosorb-6 device (Quantachrome Corporation, Florida, USA). Prior to the analysis, anodized samples were degassed at 250°C for 2 h. Pore size distribution of anodized samples was obtained using Barrett, Joyner and Halenda method (BJH method).

3.1.4 Cell Culture

L929 mouse fibroblast cells (NCTC Clone 929) were cultured using a complete growth medium of High Glucose DMEM (Biosera, Nuaille, France) supplemented with 10% fetal bovine serum (FBS, Biosera, Nuaille, France) and 1% Penicillin-Streptomycin (Biosera, Nuaille, France) and incubated at 37° C in a humidified incubator with 5% CO₂. For sterilization, tantalum samples were rinsed with 70% ethanol for 30 s and then each side of the samples was exposed to UV radiation for 30 min. Prior to cell seeding, samples were rinsed with 1x phosphate buffered saline (PBS).

3.1.5 Cell Proliferation

Sterile tantalum samples were inoculated with L929 fibroblasts at a density of 10,000 cells per sample using 30 µl complete growth medium and cells were allowed to adhere. After 4 h, 470 µl of complete growth medium was further added into each well. At 2nd and 4th days *in vitro*, growth media to culture the cells were replaced with fresh ones. At 1st, 3rd and 5th days *in vitro*, MTT assay was performed for spectrophotometric analysis of cellular density on the surfaces. Prior to MTT assay, growth media were aspirated and the samples were rinsed with 1xPBS. Afterwards, 500 µl complete growth medium containing 10% (v/v) MTT reagent was added onto each sample and the samples were incubated at 37°C/ 5% CO₂ for 3.5 h. Once incubation was complete, MTT reagent solutions were aspirated and 500 µl DMSO was added onto each sample to dissolve formazan crystals formed by viable cells. 100 µl of the solution from each sample containing dissolved formazan crystals were transferred to a 96 well plate and their absorbance values were recorded using Microplate Absorbance reader (Bio-rad, Hercules, California) at 570 nm (reference wavelength-750 nm). The absorbance values of blank samples without any cells were subtracted from the obtained absorbance values. The number of cells adherent on each sample was determined by comparing the absorbance values to a standard curve

constructed at the beginning of each trial. Cell proliferation experiments were repeated in triplicate.

3.1.6 Cellular Imaging

For cellular imaging, cells were seeded onto tantalum samples at a cell density of 1,500 cells/cm² and cultured in complete growth medium under standard cell culture conditions for 72 h. After 72 h, culture media were aspirated and the samples were rinsed twice with 1xPBS. Then, fibroblasts were fixed using 4% paraformaldehyde (Sigma-Aldrich). To permeabilize the cells, samples were incubated in 0.1% Triton X-100 for 5 min, followed by rinsing the samples with 1xPBS. Cells were blocked with %1 bovine serum albumin (Biosera, Nuaille, France) solution for 20 min. Actin filaments of the cells were stained with Alexa Fluor 488 Phalloidine solution for 20 min, followed by counterstaining the nuclei of the cells with (4',6-diamidino-2-phenylindole) (DAPI) solution for 3 min. Once staining was completed, samples were rinsed three times with 1xPBS. Cellular images were captured with a Leica DM2500 microscope (Wetzlar, Germany) at 20x magnification using appropriate cubes and filters for each stain.

3.1.7 Cell Morphology

Cellular morphologies on tantalum samples were analyzed using SEM at 3 days *in vitro*. Prior to imaging, adherent cells were fixed with 3% glutaraldehyde solution for 10 min, followed by dehydration of the cells with 30, 50, 70, 90 and 100% ethanol, respectively, for 10 min each. Afterwards, samples were covered with hexamethyldisilazane (HDMS, Sigma-Aldrich) and left overnight to dry. The dried samples were coated with gold-palladium using Quorum SC7640 high resolution sputter coater (Lewes, United Kingdom) to prevent charge build-up during SEM imaging.

3.1.8 Statistical Analysis

The statistical analysis of data was performed with SPSS software (Armonk, New York) using analysis of variance (ANOVA). One-way ANOVA with Tukey's test were chosen for the data analysis.

3.2 Results

The surface morphology of non-porous tantalum sample, along with tantalum samples anodized at 30 V for 5, 10, 15 and 20 min are displayed in Fig. 3.1a-e. SEM images showed formation of nanoporous morphologies on the surfaces of anodized tantalum samples. It was observed that the average pore size of the anodized samples increased in parallel with an increase in anodization duration (Fig. 3.1f). Upon anodizing the tantalum samples for 5, 10, 15 and 20 min, average pore sizes of 25 ± 4 , 35 ± 5 , 44 ± 6 and 65 ± 9 nm were obtained, respectively, which were named as NPT25, NPT35, NPT45 and NPT65, respectively. In order to reveal the formation mechanism of nanoporous tantalum oxide layers, I-t graph was recorded up to 20 min anodization time and displayed in Fig. 3.1g. In this graph, 4 distinct regions (a, b, c and d) were observed. In part a, the current in the electrochemical cell decreased swiftly for 30 s until reaching the minimum current at region b. Afterwards, the current started to increase gradually for nearly 15 min in region c. Upon reaching the maximum point at region d, the current decreased once again until 20 min of anodization time. To observe morphology of the anodized surface layers, NPT25 (minimum pore size) and NPT65 (maximum pore size) were investigated with TEM and the micrographs were displayed in Fig. 3.1h-i. TEM micrographs confirmed formation of nanoporous morphologies on the surfaces of anodized tantalum samples. SAED patterns shown in the insets identified an amorphous structure for the anodized oxide layers. This result was in-line with literature where XRD pattern of anodized coral-like tantalum oxide did not express any peaks and indicated amorphous nature of the anodized tantalum surfaces [61].

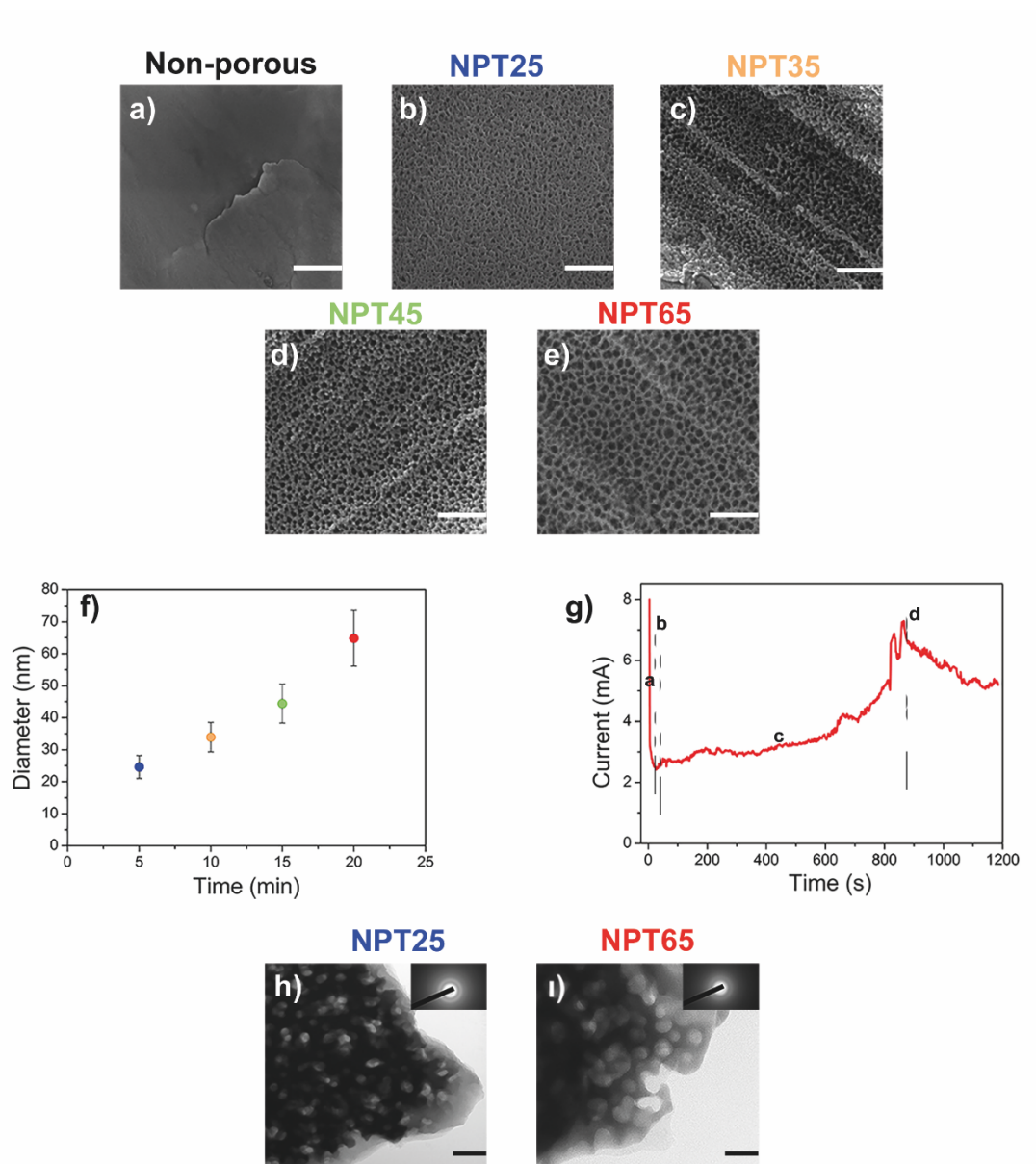


Figure 3.1. SEM micrographs of a) non-porous tantalum and nanoporous tantalum oxide surfaces having b) 25, c) 35, d) 45 and e) 65 nm average pore size. Scale bars are 500 nm. f) Increase in the average pore size of nanoporous tantalum oxide surfaces with increased anodization duration. Values are mean \pm SE, $n=3$. g) Current-time graph obtained during anodization of tantalum. Bright-field TEM images of h) NPT25 and i) NPT65 samples. Insets show SAED patterns of these samples. Scale bars for h) and i) are 50 nm.

Sessile drop water contact angle results of nanoporous tantalum oxide samples are displayed in Fig. 3.2a. Contact angles of non-porous, NPT25, NPT35, NPT45 and NPT65 surfaces were measured to be $95^\circ \pm 1^\circ$, $57^\circ \pm 5^\circ$, $63^\circ \pm 8^\circ$, $130^\circ \pm 7^\circ$ and $133^\circ \pm 9^\circ$, respectively. NPT25 and NPT35 samples were hydrophilic compared to non-porous tantalum. However, NPT45 and NPT65 were more hydrophobic compared to all other samples. It was clear that hydrophobicity of the anodized tantalum samples increased with an increase in the average pore size of the tantalum oxide surfaces. In Fig. 3.2b and c, BET analysis results of NPT25 and NPT65 samples are shown. BET analyses were in-line with SEM characterization and revealed the presence of micro and mesopores on the surfaces of the anodized samples. Fig 3.2b and c revealed typical V isotherms with H3 type hysteresis loops according to International Union of Pure and Applied Chemistry (IUPAC) [62]. Hysteresis loops showed that NPT25 samples were more porous and the insets in Fig 3.2b and c indicated that NPT25 samples had more micropores compared to NPT65 samples.

In Fig. 3.3a-e, high-resolution XPS spectra of Ta4*f* and O1*s* peaks are displayed. For non-porous tantalum, Ta4*f*_{7/2} and Ta4*f*_{5/2} peaks appeared at 21.6 and 23.5 eV, respectively, which were characteristic peaks of metallic tantalum (Fig. 3.3a) [59]. In Fig. 3.3b and d, Ta4*f* spectra of NPT25 and NPT65 samples were displayed, respectively. Ta4*f* spectra revealed two peaks at 26.2 eV for Ta4*f*_{7/2} and at 28.1 eV for Ta4*f*_{5/2} with a spin-orbit splitting of 1.9 eV. These peaks appeared at the same binding energy for both samples and indicated the formation of Ta₂O₅ on anodized nanoporous surfaces. The binding energies of these two peaks were also in good agreement with literature for Ta₂O₅ [60]. XPS analysis also revealed presence of oxygen on the anodized surfaces. O1*s* spectra of NPT25 and NPT65 samples (Fig. 3.2c and e) revealed two peaks at 530.3 and 530.2 eV for NPT25 and NPT65, respectively. These peaks belonged to Ta₂O₅, while deconvolution of the peaks revealed Ta-OH at 531.2 and 532.1 eV for NPT25 and NPT65 samples, respectively [64,65].

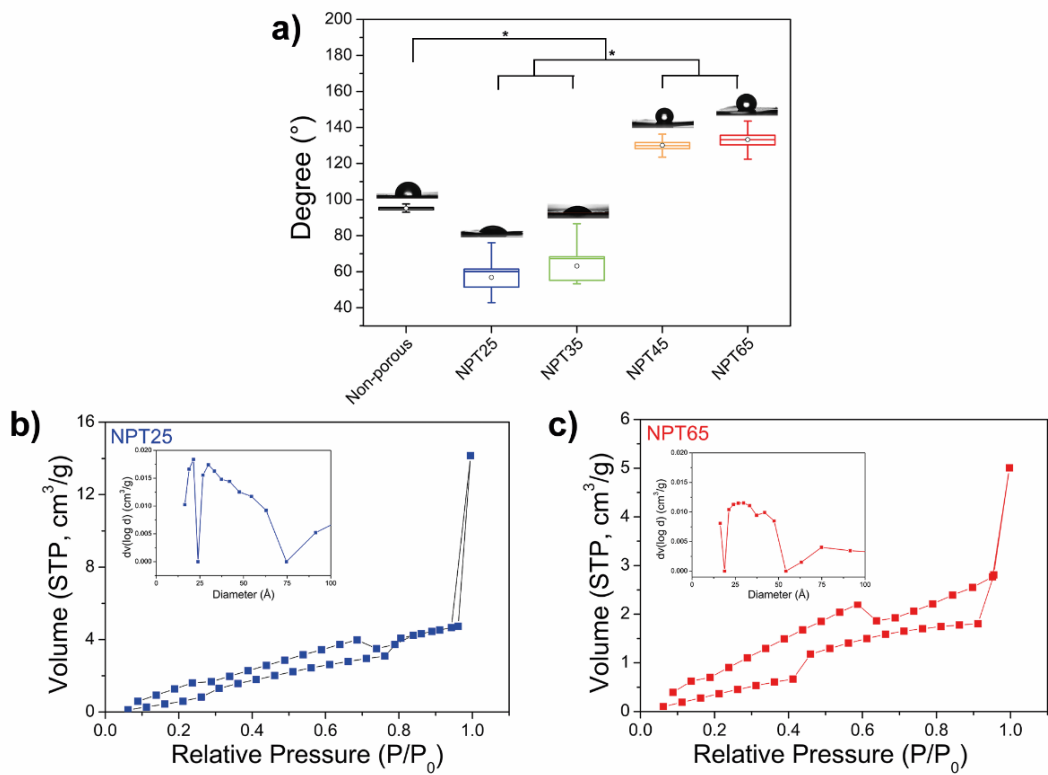


Figure 3.2. a) Sessile drop water contact angles of non-porous Ta and anodized nanoporous Ta oxide surfaces. * $p < 0.05$ compared to other groups, values are mean \pm SE, $n=3$. N_2 gas absorption-desorption hysteresis and pore size distribution of b) NPT25 and c) NPT65 samples.

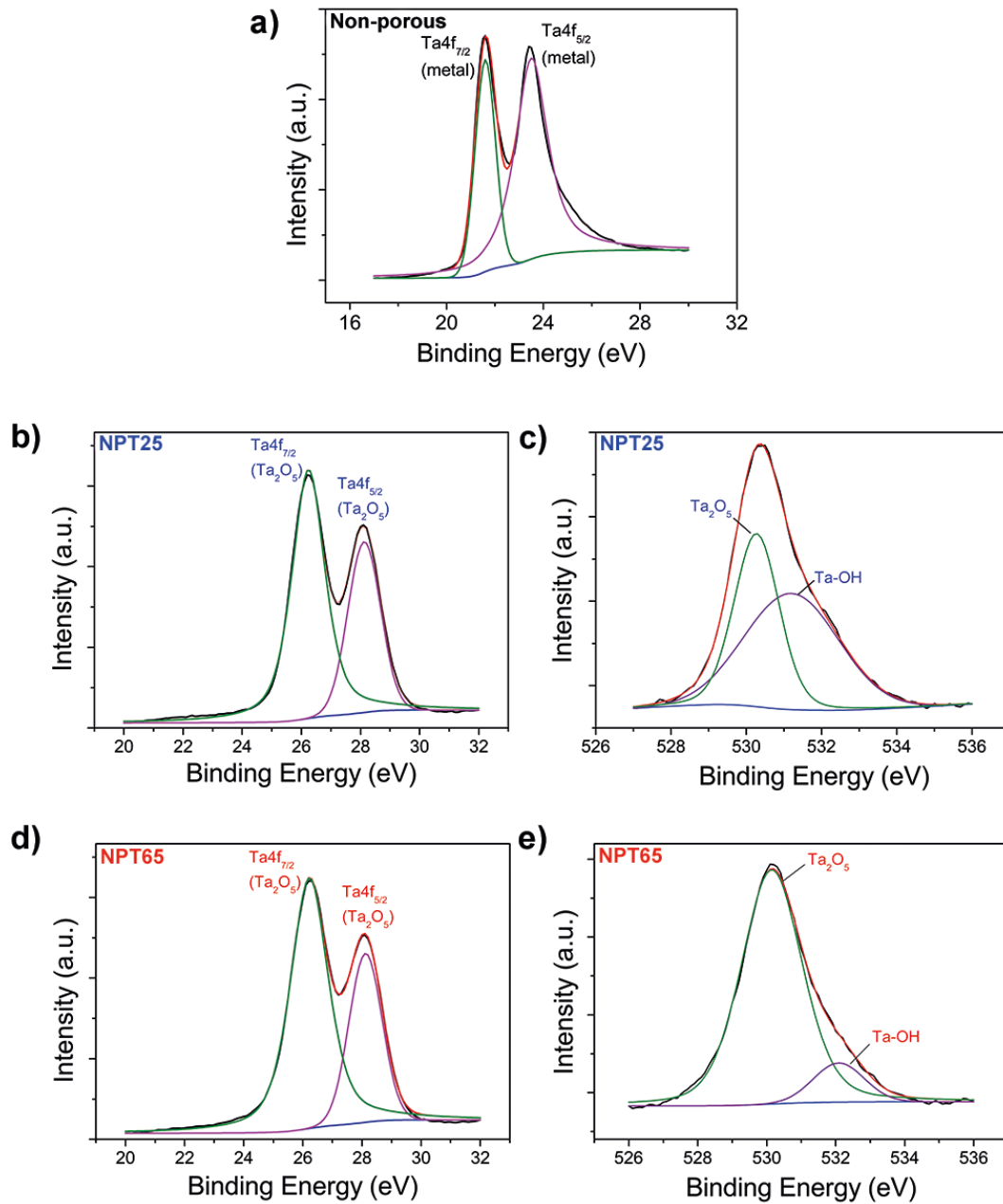


Figure 3.3. High resolution XPS spectra of a) non-porous tantalum, b) and c) NPT25 and d) and e) NPT65 samples showing a), b) and d) Ta4f and c) and e) O1s peaks.

In Fig. 3.4, AFM images and the corresponding roughness profiles and root-mean-squared (rms) roughness values are displayed. Nanophase rms roughness values were found to be 41 ± 2 , 60 ± 4 and 86 ± 4 nm for non-porous, NPT25 and NPT65 samples, respectively. Additionally, surface area of non-porous, NPT25 and NPT65 were found to be 1.3 ± 0.1 , 1.5 ± 0.1 and 1.7 ± 0.04 μm^2 , respectively. For the case of micro-phase roughness, rms values of non-porous tantalum, NPT25 and NPT65 samples were measured to be 0.57 ± 0.07 , 0.32 ± 0.01 and 0.37 ± 0.02 μm , respectively. These results showed that micro-phase roughness values decreased upon the anodization of tantalum samples and the anodized nanoporous tantalum oxide samples had a smoother surface in the micrometer scale compared to non-porous tantalum. On the other hand, anodization process increased nanophase roughness and surface area of the samples, which were documented to enhance cell-surface interactions [51,66,67]. Since resolution of the tip was not appropriate to observe the pores on the anodized tantalum samples, surface morphologies of the NPT25 and NPT65 could not be observed on 2D AFM images.

MTT results for fibroblast cells on non-porous, NPT25 and NPT65 samples are given in Fig. 3.5. At the 1st day *in vitro*, fibroblast cellular density on the NPT25 was higher compared to non-porous tantalum ($p < 0.05$), while no difference was observed between NPT25 and NPT65 samples. At the 3rd day *in vitro*, cellular density on NPT25 was significantly higher compared to non-porous and NPT65 ($p < 0.05$), while similar cellular density was observed for non-porous tantalum and NPT65. At the 5th day *in vitro*, the lowest cell density was observed on non-porous tantalum and nanoporous tantalum oxide surfaces improved cellular proliferation independent of the nanopore feature size. Fluorescence microscopy images of fibroblast cells at 3 days *in vitro* on non-porous, NPT25 and NPT65 samples are shown in Fig. 3.5b, c and d, respectively. Cells on NPT25 were spread more (2.95×10^{-5} mm^2/cell) than NPT65 (2.69×10^{-5} mm^2/cell) and non-porous tantalum (2.55×10^{-5} mm^2/cell). In fact, among the investigated surfaces in this study, non-porous tantalum showed the least fibroblast spreading. The aspect ratios of the cells were calculated to be 1.2, 1.6 and 2.1 for non-porous, NPT25 and NPT65, respectively, further indicating the

differences between cellular morphologies on these samples. Cell morphologies and cell-surface interactions were further investigated with SEM and micrographs are displayed in Figure 3.5e, f and g. Similar to fluorescence microscopy images, cells on NPT25 and NPT65 had greater cell spreading compared to non-porous tantalum.

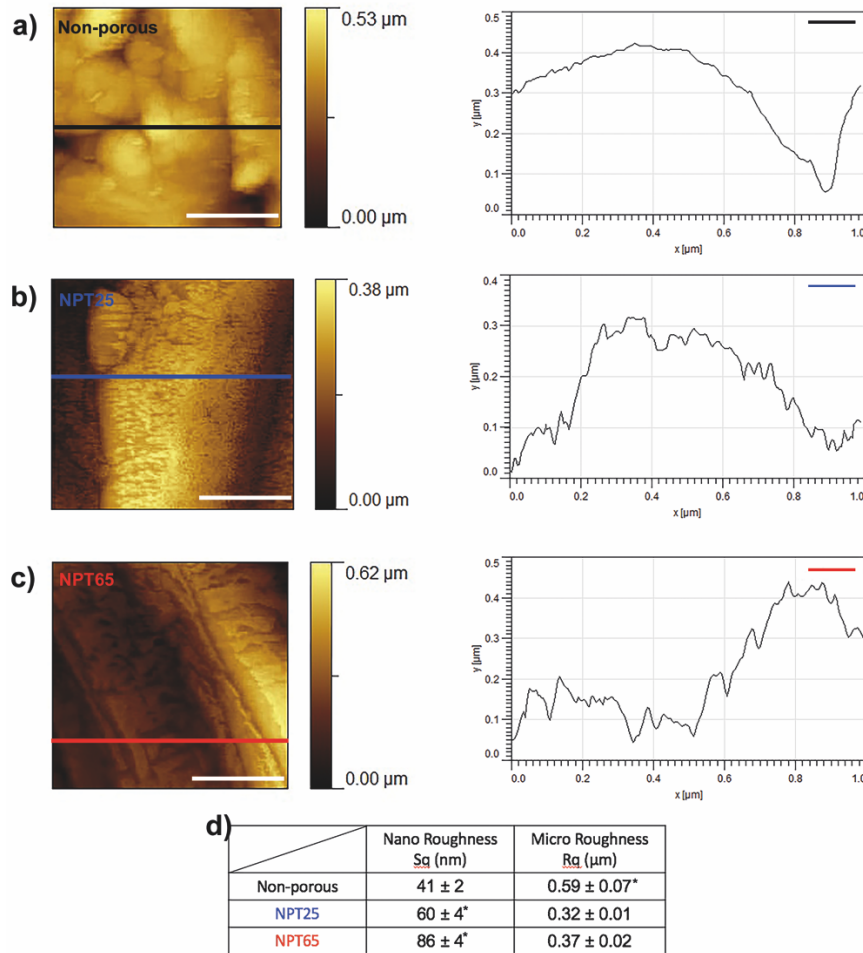


Figure 3.4. AFM micrographs and line scan profiles of a) non-porous, b) NPT25 and c) NPT65 samples. d) Nanophase and microphase roughness values of non-porous, NPT25 and NPT65 samples. * $p < 0.05$ compared to all others, values are mean \pm SE, $n=3$. Scale bars for AFM micrographs are 400 nm.

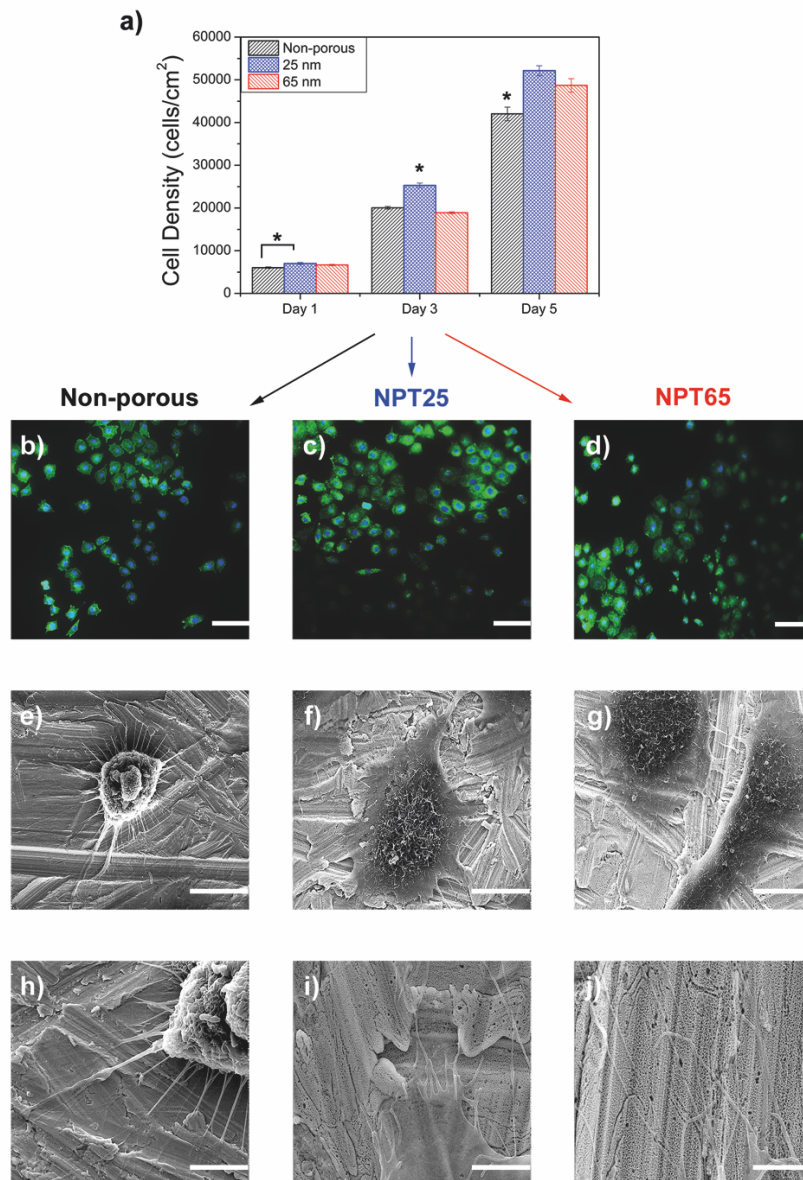


Figure 3.5. a) Fibroblast density on tantalum samples up to 5 days *in vitro*. Data are mean \pm SE, * $p < 0.05$ compared to all other samples. Actin (green) and nuclei (blue) stained images of fibroblasts cultured on b) non-porous, c) NPT25 and d) NPT65 samples. Scale bars are 50 μm . SEM images of fibroblasts cultured on e) non-porous, f) NPT25 and g) NPT65 samples. Scale bars are 10 μm . Higher magnification SEM images of fibroblasts cultured on h) non-porous, i) NPT25 and j) NPT65 samples were given. Scale bars are 5 μm for h), 1 μm for i) and j).

3.3 Discussion

3.3.1 Fabrication of Nanoporous Tantalum Oxide Surfaces

During the anodization process of tantalum, the competition between the tantalum oxide layer formation inside the electrolyte and the acid induced dissolution reactions led to the formation of nanostructured surface features. In this study, the electrolyte concentration and the water content of the electrolyte were the critical parameters to obtain the nanoporous surface features. The electrolyte needed to be concentrated enough to promote the right concentration of F^- ions to partially dissolve the readily formed oxide layer to form the nanopores on the surface, while simultaneously oxidize the surfaces under the applied potential to promote tantalum oxide layer formation. It should be noted that during optimization of anodization parameters to fabricate nanoporous surface features, a more concentrated electrolyte promoted higher etching rates and led to the formation of nanotubular features, whereas a less concentrated electrolyte promoted formation of a compact oxide layer. Upon the increase of anodization duration from 5 to 20 min, fluoride ions migrated deeper into the tantalum matrix and interacted with tantalum for a longer duration to dissolve the oxide layer, and thus led to an increase in the average pore size of the anodized nanoporous surfaces.

The formation mechanism of nanopores during anodization process could be explained using the I-t curve provided in Fig. 3.1g. At the beginning of anodization process, a strong surge of current occurs, resulting in formation of a barrier layer. However, it cannot be captured by the voltage source since it happens suddenly. After that, (part a) the dramatic decrease of current was observed due to formation of a compact Ta_2O_5 layer formation, which prevented current flow through the system. In region b, small pits started to appear on tantalum oxide and grew into porous structures in different orientations due to the dissolution reaction of fluoride ions. In part c, current passing through the electrochemical cell increased due to the dissolution effect of fluoride ions, which also migrated further into the barrier oxide.

After that, maximum current was reached. Due to limited diffusion of electrolyte into the pores, it started to decrease again towards reaching an equilibrium between oxide formation and dissolution reactions. For NPT25 sample, only regions of a, b and some portion of c are observed. This led to the formation of barrier oxide layer and small nanopores appeared on the surfaces [68,69]. These pores are visible in Fig. 3.1b and h. It is important to note that formation of multiple layers of stacked nanoporous rather than a single nanoporous layer was observed on the NPT 25 samples (Fig. 3.1h). However, for the NPT65 samples, anodization duration was long enough to observed four distinct regions in the I-t curve. The longer anodization duration allowed more time for the rearrangement and coalescence mechanism of nanopores in region d of I-t curve, which led to the formation of larger nanopores. This was also clear in Fig. 3.1e and i, where the surface oxide layer had larger nanopores.

Nanoporous oxide layers obtained on the surfaces of NPT25 and NPT35 samples enhanced the hydrophilicity of the tantalum samples, as evidenced in Fig. 3.2 [66]. Interestingly, NPT45 and NPT65 samples exhibited more hydrophobic characteristics compared to non-porous sample in spite of the hydrophilic nature of the Ta₂O₅ layer grown on their surfaces during anodization. Wettability and water contact angles on rough surfaces could be explained with Cassie-Baxter model, where water molecules are not in full contact with the underlying surface, yet water could only contact the peak points of the underlying surface due to the entrapment of air molecules in the surface cavities [71]. Wettability results for NPT45 and NPT65 samples could be explained with the Cassie-Baxter model. It was possible that the increase in air/water contact area due to the presence of entrapped air bubbles inside the larger nanopores influenced water contact angles of the NPT45 and NPT65 samples and led to an increase in sample hydrophobicity. It is important to note that pore size highly influences wettability. Similar trends were also observed in literature where increase in pore size led to higher water contact angles in anodized nanoporous aluminum structures [72].

AFM results indicated increase in nanophase surface roughness and the total surface area of the samples increased after anodization. The increase in nanophase roughness and sample surface area could be attributed to the formation of nanopores on the anodized surfaces and highlighted the effect of anodization on the surface topography in the nanoscale regime. Increased nanophase surface roughness and surface area were also observed in literature for other anodized metals and proposed to facilitate interactions with the cells surrounding the implant [66,67]. Having this said, anodization process was observed to smoothen the tantalum metal surface in the micro-scale. The formation of nanofeatures were proposed to start at concave regions of the surface due to having higher charge density, which increased the electrical field around these points and led to the localized dissolution around these points [73]. Localized dissolution of the concave regions smoothen the micro-phase topography of the samples independent of the nanopore dimension.

3.3.2 Fibroblast Proliferation on Nanoporous Tantalum Oxide Surfaces

For the NPT25 sample, the chemistry of its surfaces was altered during anodization to form Ta_2O_5 . In addition, NPT25 sample expressed the highest hydrophilicity, while its nanophase surface roughness and total surface area were higher compared to non-porous tantalum. All these changes in the surface properties of tantalum to form 25 nm sized nanopores favored fibroblast adhesion, proliferation and spreading since the surface properties of tantalum, *i.e.* surface chemistry, topography, hydrophobicity and surface area, were important factors influencing cellular adhesion and proliferation [74]. For instance, it was revealed that surface topography played a critical role for the adhesion of cells onto tantalum-based implant surfaces. Since nanofeatured tantalum oxides have higher surface area compared to their nanosmooth counterparts, they promote cellular adhesion, spreading and proliferation to a higher extend on nanofeatured surfaces [75,76]. Also, it was observed in the literature that hydrophilic surfaces promoted higher fibroblast adhesion and spreading compared to hydrophobic ones [77]. Thus, NPT25 surfaces

exhibited higher cell density compared to non-porous tantalum at 1, 3 and 5 days *in vitro*. In addition, the fibroblast spreading and cell density on NPT25 surfaces were greater than NPT65 at the 3rd day *in vitro*, yet no statistical significance was observed for cell density at the 5th day *in vitro* between the nanoporous surfaces. It was possible that reaching confluency at an early time point on NPT25 led to a decrease in cellular proliferation rate and allowed elimination of the statistical difference between NPT25 and NPT65 at 5 days *in vitro*. It should be noted that NPT65, similar to NPT25, had Ta₂O₅ on the sample surfaces. Furthermore, the nanophase surface roughness and surface area were found to be the highest for NPT65 among the investigated sample groups. Even though, the hydrophilicity of NPT65 was lower compared to non-porous tantalum and NPT25 samples, cell density on NPT65 was significantly higher at 5 days *in vitro* compared to non-porous tantalum samples. It was clear that hydrophobicity of the anodized nanoporous surfaces had an influence on the adhesion and proliferation of fibroblast cells, yet formation of an oxide layer and induction of nanophase topography via anodization were also influential parameters on the fibroblast functions and could enhance adhesion and proliferation of fibroblast cells on nanoporous tantalum oxide surfaces. To conclude, in this study, tantalum was anodized to improve its biological properties and the findings revealed that nanoporous tantalum oxide surfaces having 25, 35, 45, and 65 nm pore sizes could be fabricated using an aqueous HF:H₂SO₄ solution at 30 V for 5, 10, 15 and 20 min, respectively. Surface properties, including chemistry, topography, hydrophilicity and total porosity, could also be altered by anodization depending on the anodization parameters. In addition, this study revealed -for the first time- that fibroblast adhesion and proliferation can be enhanced on anodized nanoporous tantalum oxide samples and fibroblast cells spread more on the anodized surfaces compared to non-porous tantalum. It was concluded that surface modification of tantalum in the nanoscale via anodization could potentially be used to fabricate nanoporous oxide surfaces, which further enhance fibroblast proliferation and cell-surface interaction. This study provided the first evidence for nanoporous tantalum oxide surfaces to be a promising candidate for use in biomaterial applications.

CHAPTER 4

CONTROLLING THE NANOFEATURE SIZE AND MORPHOLOGY OF ANODIZED TANTALUM OXIDE SURFACES FOR ENHANCED OSTEObLAST INTERACTIONS

In literature, there are promising findings for the use of nanotubular tantalum surfaces in orthopedic applications. However, a thorough study investigating the anodization parameters to control nanophase surface morphology and feature size, along with assessing the interaction of anodized surfaces with bone cells is missing. Thus, in this study, oxide-based surface features having three distinct morphologies, namely nanotubular, nanodimple and nanocoral, having feature sizes specifically tailored between 20 to 140 nm were fabricated via anodization onto tantalum surfaces. Afterwards, human osteoblasts were interacted with these surfaces to investigate the influence of anodized tantalum oxide surface morphology and feature size on cellular functions.

4.1 Materials and Methods

4.1.1 Sample Preparation

A tantalum foil (99.95% purity, Alfa Aesar, Haverhill, Massachusetts) was cut into 1 x 1 cm samples, followed by sonicating the samples successively in acetone, 70% ethanol and distilled water each for 15 min. A two-electrode electrochemical system was used for anodization where a platinum mesh (Thermo Fisher Scientific, Lancashire, UK) was the cathode and a surface cleaned tantalum sample was the anode. Copper wires were used to connect anode and cathode to the power supply (Genesys 300V/5, TDK Lambda, Achern, Germany). Tantalum samples were anodized using 9:1 H₂SO₄ (95-97%, Sigma Aldrich, St. Louis, Missouri):HF (38-40%, Merck, Kenilworth, New Jersey) (v/v) electrolyte to obtain nanotubular surface

features. Anodization potentials were altered from 10 to 55 V and the anodization duration was 1 min for all nanotubular samples. 9:1 H₂SO₄:HF (v/v) + 5 vol% Dimethyl Sulfoxide (DMSO, > 99.9 %, Sigma Aldrich, St. Louis, Missouri) electrolyte was used to fabricate nanodimple surface features on tantalum. The applied potentials ranged between 10 to 35 V and the anodization durations were set between 10 to 30 min. To fabricate the nanocoral surface morphology, samples were anodized using 1 M H₂SO₄ + 3.3 wt% NH₄F (> 98%, Merck, Kenilworth, New Jersey) electrolyte. The applied potential was kept at 20 V and the anodization durations controlled from 60 to 150 min. Anodization experiments were carried out between 4 to 10 °C to fabricate nanotubular and nanodimple surface morphologies, whereas nanocoral surface morphology was fabricated at room temperature. At the end of the anodization process, all samples were rinsed with ultrapure water and dried at ambient conditions.

4.1.2 Surface Characterization

Morphology of the surfaces was investigated with a scanning electron microscope (SEM, FEI, Nova Nano 430, Brno, Czech Republic) using a secondary electron detector. Accelerating voltage was kept at 20 kV. Prior to the SEM analysis, Quorum SC7640 high-resolution sputter coater (Lewes, United Kingdom) was used to coat anodized surfaces with a thin layer of Au-Pd. For quantitative analysis of the feature dimensions, size measurements were completed from 90 different surface features using ImageJ 1.51 software (National Institute of Health, Bethesda, Maryland). Size measurements were repeated in triplicate. To characterize the crystal structure of the nanotubular and nanocoral samples, transmission electron microscopy (TEM; JEM 2100F, JEOL, Tokyo, Japan) analysis was conducted. Prior to TEM analysis, oxide layers on the surface of the anodized tantalum samples were mechanically removed and suspended in ethanol. Afterwards, samples were put into holey carbon coated copper grids and allowed to dry for 10 min. An accelerating voltage of 200 kV was used during image capture. Bright-field, high resolution (HR) and selected area

electron diffraction (SAED) modes of TEM were used to characterize the samples. Hydrophobicity of the samples was measured using a goniometer (EasyDrop, KRÜSS GmbH, Hamburg, Germany). 3 μ l ultrapure water was dropped onto each sample and the contact angles with the surfaces were measured. Contact angle measurements were repeated in triplicate for each sample. Atomic force microscopy (Veeco, Multimode V, Santa Barbara, California) analyses were conducted to characterize surface roughness of the samples. Surface topography of the samples was investigated in tapping mode using a silicon AFM tip having 10 nm radius. 1 x 1 μ m fields were scanned for each sample at 1Hz scanning rate. Surface area and root-mean square roughness values of the samples were calculated using Image Plus software (Peseux, Switzerland). Surface chemistries were examined using X-ray photoelectron spectroscopy (PHI, 5000 Versa Probe, Minnesota, USA) with monochromatic Al K_{α} X-ray source. Prior to XPS analysis, sample surfaces were sputtered at 3 keV for 3 min. For XPS analysis, approximately 7 Pa vacuum pressure was specified. Scans for Ta 4*f*, O 1*s* and C 1*s* orbitals were collected from a spot diameter of 50 μ m. Electrostatic charging of the samples were corrected using C 1*s* peak at 284.5 eV as a reference. Deconvolution of the Ta 4*f*_{7/2}, Ta 4*f*_{5/2} and O 1*s* peaks were completed using XPS Peak41 software.

4.1.3 Cell Culture

Human bone cells (hFOB 1.19, ATCC CRL-11372) were cultured using Dulbecco's Modified Eagle's Medium (DMEM, Sigma Aldrich, St. Louis, Missouri) supplemented with 10% fetal bovine serum (FBS, Sigma Aldrich, St. Louis, Missouri), 1% Penicillin-Streptomycin (Sigma Aldrich, St. Louis, Missouri) and 1% L-Glutamine (Sigma Aldrich, St. Louis, Missouri) under standard cell culture conditions (37° C and 5% CO₂ atmosphere). Prior to cell seeding, tantalum samples were sterilized with 70% ethanol, followed by exposing both sides of the samples to UV light for 30 min.

4.1.4 Cellular Proliferation

hFOBs were seeded onto sterile tantalum samples at a density of 20,000 cells/cm² using 60 µl complete growth medium and cells were allowed to adhere for 4 h. Afterwards, 440 µl complete growth medium was added onto each sample and cells were cultured up to 5 days *in vitro* under standard cell culture conditions (37° C and 5% CO₂ atmosphere). MTT assay was conducted at 1st, 3rd and 5th days of culture to determine cellular density on the sample. Prior to MTT analysis, culture medium was removed, followed by rinsing the samples with 1xPBS (phosphate buffered saline) and adding 500 µl growth medium containing 10% MTT reagent (v/v) onto each sample. Samples treated with the MTT reagent were incubated for 4 h, followed by aspiration of the MTT solution and incorporation of 500 µl 0.1 M HCl solution in isopropanol onto each sample to dissolve formazan crystals formed inside the cells. Once all the crystals were dissolved, 250 µl isopropanol solution from each sample was transferred to a 96 well plate and absorbance of the solutions were read at 570 nm (reference wavelength-750 nm) using Thermo Scientific Multiskan Go microplate absorbance reader (Waltham, Massachusetts). The absorbance values of blank samples (without any cells) were subtracted from the obtained absorbance values. The number of cells adherent on each sample was determined by using a standard curve constructed using known number of cells at the beginning of each trial. MTT experiments were repeated in triplicate.

4.1.5 Protein Adsorption

500 µl solution of 11% FBS in 1xPBS was added onto sterile tantalum samples and incubated at 37°C/ 5% CO₂ for 4 h. At the end of 4 h, FBS solution was aspirated, followed by rinsing the samples with 1xPBS and transferring them into fresh well plates. To remove the adsorbed proteins, 300 µl solutions of 8 M Urea (Sigma Aldrich, St. Louis, Missouri), 0.1 M Trisbase (Sigma Aldrich, St. Louis, Missouri) and 0.01 M 1,4-Dithiothreitol (DTT, Thermo Scientific, Waltham, Massachusetts)

were added onto each sample and the samples were put on a plate shaker (IKA, Rocker 3D, Staufen, Germany) for 20 min at 80 rpm. 50 µl solution containing the removed proteins was transferred to a 96 well plate and 250 µl Bradford solution was incorporated. Absorbance values of the solutions were recorded at 595 nm using microplate absorbance reader. Absorbance values of blank samples were subtracted from the obtained values. Adsorbed protein concentration was calculated using a standard curve constructed using Bovine Serum Albumin (BSA, Sigma Aldrich, St. Louis, Missouri) standard. Protein adsorption experiments were repeated in triplicates.

4.1.6 Cellular Imaging

hFOBs were seeded onto sterile tantalum samples at a density of 10,000 cells/cm² and incubated at 37°C/ 5% CO₂ for 3 days. After 3 days *in vitro*, culture media were aspirated, and cells were fixed using 4% paraformaldehyde solution for 30 min at room temperature. The fixed cells were permeabilized with 0.2% Triton X-100 for 30 min and blocked with 5% BSA for 30 min. Afterwards, rabbit monoclonal anti-vinculin antibody (Abcam, Cambridge, United Kingdom) diluted at a concentration of 1:200 was used to target vinculin protein for 90 min, followed by adding goat anti-rabbit polyclonal secondary antibody IgG linked with Alexa Fluor 488 (Abcam, Cambridge, United Kingdom) diluted at a concentration of 1:1000 in 0.5% BSA onto each sample for 1 h to target the primary antibody. Once immunostaining for vinculin was complete, actin fibers were stained with red fluorescence phalloidin prepared at 1:200 dilution factor (Abcam, Cambridge, United Kingdom) for 1 h at room temperature. Lastly, 4',6-Diamidino-2-Phenylindole, Dihydrochloride (DAPI) solution diluted in 0.5% BSA at a concentration of 1:40,000 was added onto the samples and incubated for 30 min. Cells were rinsed with 1xPBS at every step during this staining protocol. Cellular images were captured with Zeiss Confocal Microscope (LSM800, Germany) using the appropriate cubes and filters for each fluorophore.

4.1.7 Cellular Morphology

hFOBs were seeded onto sterile tantalum samples and incubated for 3 days *in vitro*. After 3 days of culture, cells were fixed with 3% glutaraldehyde solution for 10 min, followed by dehydration with 30, 50, 70, 90 and 100% ethanol solutions successively for 10 min each. Dehydrated cells were treated with hexamethyldisilazane (HMDS, Sigma-Aldrich) and left to dry for 24 h. Samples were coated with gold-palladium using Quorum SC7640 high resolution sputter coater (Lewes, United Kingdom) prior to SEM imaging.

4.1.8 Statistical Analysis

SPSS software (Armonk, New York) was used for the statistical analysis of the data. One-way ANOVA with Tukey's test were applied for data analysis. P values less than 0.05 were considered statistically significant.

4.2 Results and Discussion

Surface morphologies of non-anodized and anodized samples are given in Fig. 4.1. SEM images confirmed the formation of nanotubular (Fig. 4.1.b-c), porous nanocoral (Fig. 4.1.d-e) and nanodimple (Fig. 4.1.f-g) surfaces upon anodization of tantalum under different anodization conditions. In Fig. 4.1, only the samples having minimum (Fig. 4.1.b, 4.1.d and 4.1.f) and maximum (Fig. 4.1.c, 4.1.e and 4.1.g) sized surface features are displayed. In this research, samples having nanotubular, nanocoral and nanodimple surface morphologies are abbreviated as NT, NC and ND, respectively, and the samples having minimum and maximum sized surface features were indicated with 'min' and 'max' suffix, respectively. For all NT samples, 9:1 H₂SO₄:HF solution was used as the electrolyte and the anodization duration was kept constant at 1 min. While NT-min surfaces (Fig. 4.1.b) were anodized at 10 V, 55 V potential was used to anodize NT-max surfaces (Fig. 4.1.c). When anodization

potential increased from 10 to 55 V, increase in nanotubular diameter was observed for the NT samples. The increase in nanotubular diameter was also evident comparing the bottom views of the nanotubular features (insets for Fig.4.1.b and 4.1.c). For the NC samples, 1 M H₂SO₄ + 3.3 wt% NH₄F aqueous solution was used as the electrolyte and the anodization potential was kept constant at 20 V. Similar to previously published results of our research group [55], the high water content inside the electrolyte led to the formation of a nanoporous surface morphology. In addition, comparison of these findings with our previous publication showed that the formation of nanoporous structures was independent of the F⁻ ion source used inside the electrolyte. NC-min samples were anodized for 60 min, whereas NC-max samples were anodized for 150 min. It was observed that under a constant potential, pores were growing with increased anodization duration. For the case of ND samples, 5 vol% DMSO was included inside 9:1 H₂SO₄:HF solution used for the NT samples, which decreased the conductivity of the electrolyte and allowed us to anodize for longer durations, which led to the formation of dimple surface morphologies. Both the applied potential and the anodization duration were altered during surface modification of ND surfaces, where ND-min surfaces were anodized at 10 V for 10 min and ND-max surfaces were anodized at 35 V for 30 min. Similar to nanotubular and nanocoral surface morphologies, an increase in the dimple diameters was also observed upon an increase the in anodization potential and duration.

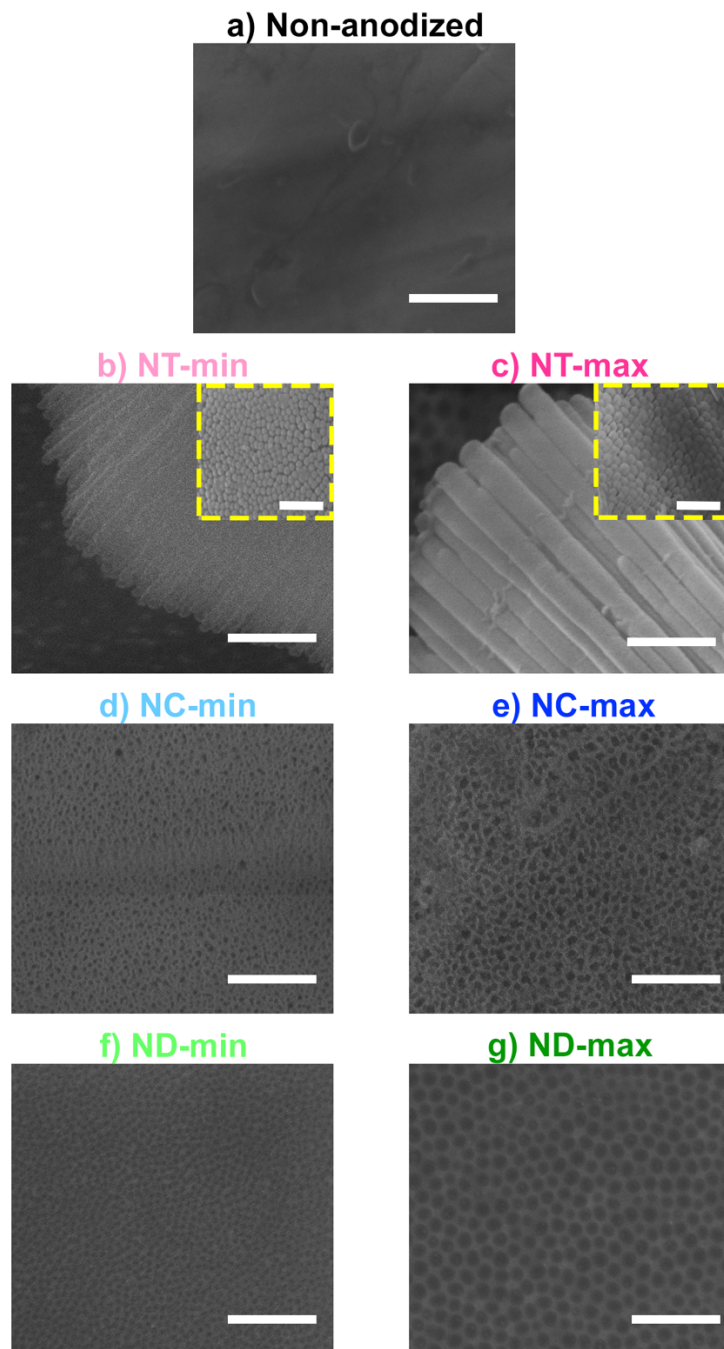


Figure 4.1. SEM micrographs of a) non-anodized, b) NT-min, c) NT-max, d) NC-min, e) NC-max, f) ND-min and g) ND-max samples. Insets for NT-min and NT-max show the bottom views of the nanotubular features. Scale bars are 500 nm.

In Fig. 4.2., the change in feature size and thickness for the anodized tantalum samples were quantitatively analyzed. As indicated in Fig. 4.2.a and 4.2.b, a linear increase in the nanotubular feature size from 30 nm to 140 nm ($R^2=0.99$) and oxide layer thickness from 0.5 μm to 8.5 μm ($R^2=0.97$) was observed upon increasing the anodization voltage from 10 V to 55 V. The increase in nanotubular feature size could be explained with the increased dissolution effect of fluoride ions upon the increase in anodization potential [78]. In addition, upon increasing the potential across the electrochemical cell, oxygen anions present in the electrolyte migrated deeper inside the oxide layer, resulting in an increase in the oxide layer thickness [79]. When image analysis was performed on NC samples, it was observed that nanocoral feature size increased linearly with anodization duration ($R^2=0.97$), where up to 6-folds increase from 20 nm to 120 nm was observed when anodization duration increased from 60 min to 150 min, as indicated in Fig. 4.2.c. Since fluoride ions present in the electrolyte could dissolve the anodized oxide layer, the prolonged interaction of the anodized oxide surface with the electrolyte led to an increased dissolution and an increase in nanocoral pore size [80]. For the case of ND samples, both the applied potential and the anodization duration were fine-tuned to alter nanodimple feature size where minimum and maximum obtained feature sizes were calculated to be 25 nm and 90 nm, respectively (Fig. 4.2d and Supp. Fig.4.11). Detailed analysis in the nanodimple fabrication parameters identified anodization potential as the leading parameter to control nanodimple feature size. Independent of the anodization duration, nanodimple size increased linearly with anodization potential (The R^2 values for 10, 20 and 30 min anodization were found to be 0.99, 0.96 and 0.97, respectively). The change in feature size with anodization potential could be explained with the formation mechanism of nanodimples, which were the remaining surface morphologies upon the detachment of nanotubular features from the surfaces. In other words, what was observed in Fig. 4.1.f and 4.1.g were the very thin, dimple shaped surface remnants of the detached nanotubular oxide arrays. Since increase in the anodization potential was correlated with increased nanotubular diameter for NT samples, larger sized dimpled morphologies were forming on the

tantalum substrates upon the detachment of nanotubular arrays having increased nanotubular diameter.

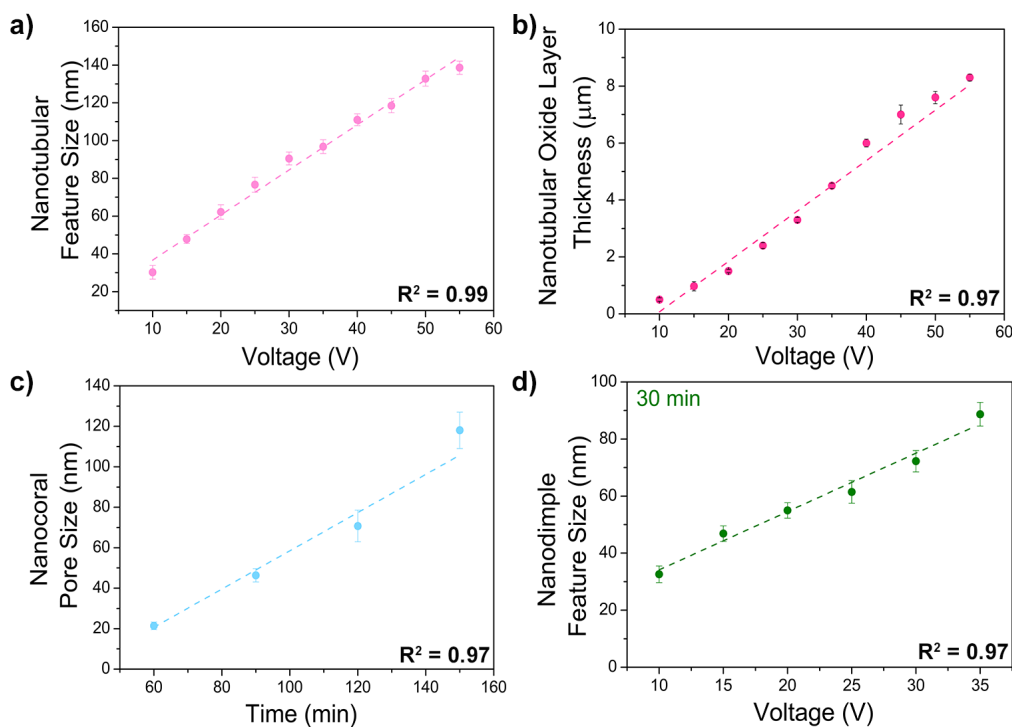


Figure 4.2. Graphs indicate a) nanotubular feature size vs. voltage, b) nanotubular oxide layer thickness vs. voltage, c) nanocoral pore size vs. anodization time, d) nanodimple feature size vs. voltage for 30 min anodization. Values are mean \pm SEM, n=3.

The current-time graphs of tantalum samples anodized to have maximum and minimum feature sizes are shown in Fig. 4.3. During an anodization process, the formation of nanofeatured surfaces typically consists of three distinct regions on their I-t curves. In the first region, current decays constantly until reaching a minimum point due to the formation of a barrier oxide layer. In the second region, field-enhanced dissolution of oxide layer starts, and small pits form on the surface of the barrier oxide layer. Gradually, these pits get larger and turn into pore structures, which leads to an increase in current. The size and number of these pores

increase in parallel with the aforementioned increase in current until the current reaches a maximum value. Finally, in the third region, current begins to decrease due to the limited ionic diffusion across thickened surface oxide layer [38]. In Fig. 4.3.a, I-t curve for the NT-min sample is displayed and the curve exhibited similar trends observed for the formation of nanotubular and nanoporous surfaces in the literature [5,81]. For NT-max sample (Fig. 4.3.b), current decreased sharply during the initial 10 s, followed by a region where the decrease in current was almost constant. In addition, small oscillations in current are evident in the I-t diagram. These oscillations could be attributed to the formation of free-standing nanotubular layers [5]. SEM investigations showed that NT-max surfaces lacked homogenous coverage of nanotubular features across their surfaces. Our observations showed that surface oxide layer started to delaminate from the tantalum substrate and formed free-standing oxide layers at potentials above 30 V (Supp. Fig. 4.12). In fact, oxide layer delamination was observed to increase with an increase in the anodization potential from 30 V to 55 V. This is why NT samples anodized at 30 V were selected for the biological studies. In Fig. 4.3.c and 4.3.d, I-t curves for the NC-min and NC-max samples are displayed, respectively, and these I-t curves show all of the 3 characteristic regions for the anodized nanoporous surfaces. Similar to the NT samples, there was an initial exponential decay in the current with time due to the formation of a compact surface oxide layer. Afterwards, as fluoride ions inside the electrolyte began to dissolve the compact oxide layer to form nanopore structures, the current across the electrochemical cell started to increase and reached a maximum value at around 3500 s, which was followed by a sharp decrease in the current to reach a local minimum. Then, the pore formation cycle would start once again, similar to the previous cycle, with an increase in current. During formation of pores, the electrical field distribution at the pore tips changes, which was shown to induce mechanical stress on porous oxide layers [82,83]. The mechanical stress building up on the oxide layers could gradually lead to the partial (or full) separation of the oxide layer from the tantalum substrate, while the on-going anodization inside the electrolyte would allow formation of another layer of porous oxide and,

eventually, led to the formation of layer-by-layer porous tantalum oxide structures shown in Supp. Fig. 4.13. In addition to the mechanical stress, the gradual building up of fluoride rich TaF₅ complex in the Ta/Ta₂O₅ interface could have contributed to the detachment of Ta₂O₅ layer from the tantalum surfaces [84]. It should be noted that delamination was becoming an issue for extended anodization durations for the NC morphology. SEM images of NC-max samples, which were anodized for the longest time among all the specimens tested in this study, showed delaminated oxide layers on their surfaces (Supp. Fig. 4.14.a and 4.14.b). For the NC-min samples, anodization duration was significantly shorter than the NC-max samples, which could have led to less mechanical stress build-up and TaF₅ formation, and thus oxide layer delamination was not observed for these samples. The I-t curves for ND-min and ND-max samples were shown in Fig. 4.3.e and 4.3.f, respectively. Similar to NT and NC samples, anodization current initially decreased and reached a minimum value. However, unlike the I-t trends observed for anodization of NT-min and NC samples, current values stayed nearly constant for the ND samples. This was in-line with literature where a constant decrease in current was correlated with the formation of stable nanotubular surfaces [38], whereas nanotubular structures were unstable under steady-state anodization currents and induced detachment of nanotubular structures [39]. The detached nanotubular structures left behind dimple surface morphologies on tantalum. It could be speculated that the build-up of TaF₅ complex at the tantalum/tantalum oxide interface led to changes in the potential distribution across the oxide layer and directed detachment of nanotubular oxide layer from the tantalum substrates [84].

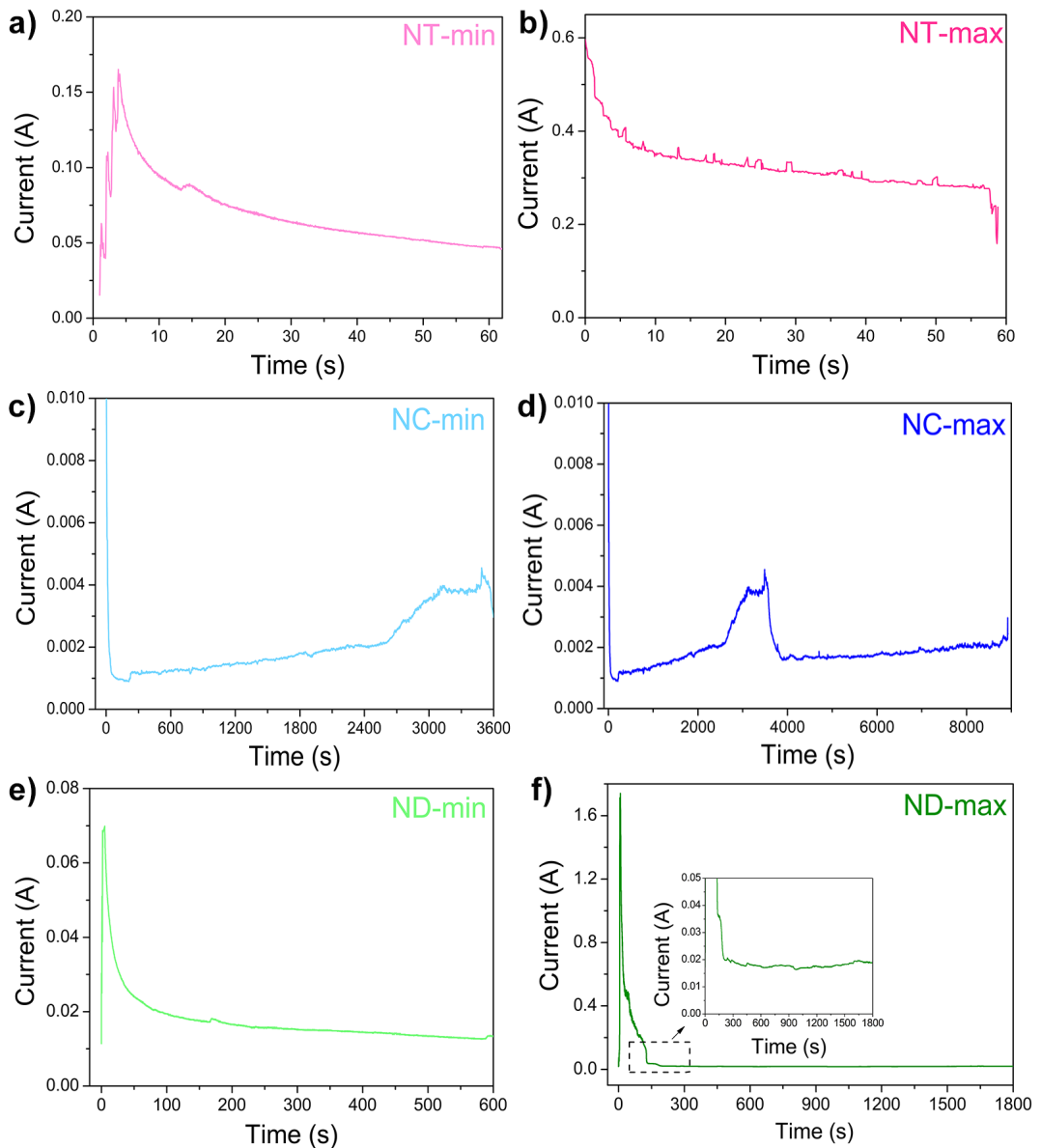


Figure 4.3. Current vs. time graphs for the anodized tantalum samples.

In Fig. 4.4, bright-field TEM micrographs of the oxide layers obtained from NT (Fig. 4.4.a and 4.4.b) and NC (Fig. 4.4.c and 4.4.d) surfaces are displayed. Fig. 4.4.a and 4.4.b further confirmed the presence of nanotubular structures on NT samples and the size difference between nanotubular features of NT-min (Fig. 4.4.a) and NT-max (Fig. 4.4.b) was evident. Similar to the NT samples, the porous nature of nanocoral samples was confirmed for NC-min and NC-max surfaces in Fig. 4.4.c and 4.4.d,

respectively. The oxide layer forming on tantalum upon the anodization was amorphous for both morphologies (insets of Fig. 4.4), which was in-line with literature findings [30, 31]. Even though internal structure of NT and NC samples were identified via TEM, a similar study could not be conducted for the ND samples. As stated previously, nanodimple morphology was obtained upon the detachment of the nanotubular oxide arrays from the tantalum surfaces during anodization where an extremely thin oxide layer remained on tantalum surfaces.

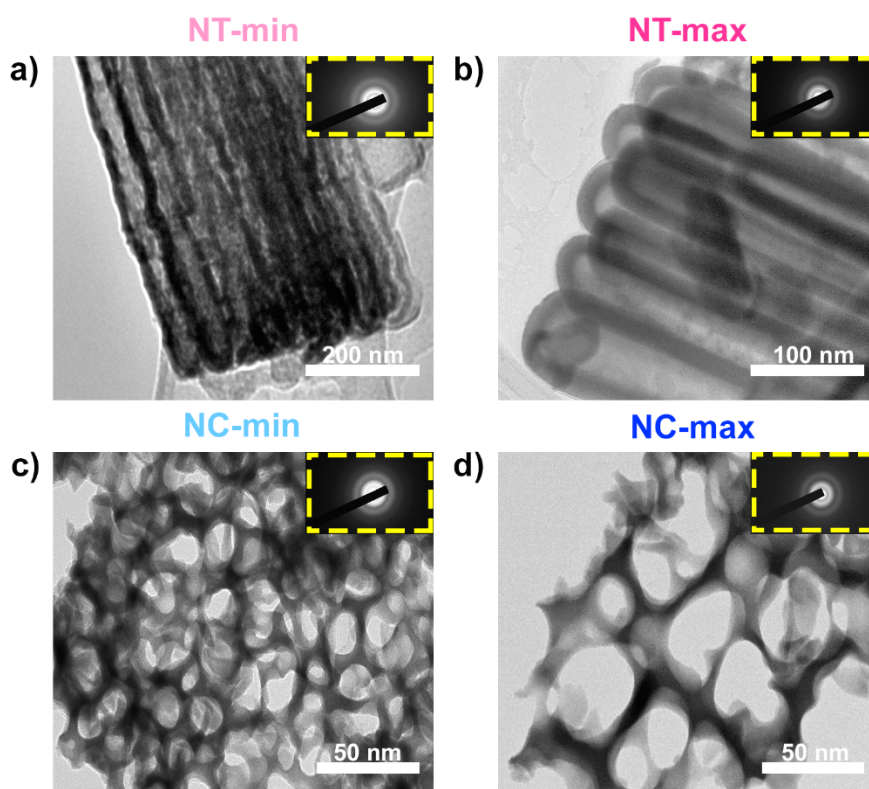


Figure 4.4. Bright-field TEM micrographs of oxide layers obtained from a) NT-min, b) NT-max, c) NC-min and d) NC-max surfaces. Insets indicate SAED patterns.

High-resolution XPS spectra of Ta4f peaks for non-anodized and anodized samples were displayed in Fig. 4.5. All peaks observed for XPS spectra of non-anodized and anodized samples were in-line with literature findings [63,64,86,87]. For the non-anodized Ta, two peaks appeared at 21.9 eV and 23.8 eV, which belonged to Ta4f_{7/2}

and $Ta4f_{5/2}$ peaks of metallic tantalum, respectively (Fig. 4.5.a). For NT-min and NT-max samples (Fig. 4.5.b and 4.5.c), aside from the metallic tantalum peaks, peaks at 29.4 eV for $Ta4f_{5/2}$ and 27.5 eV for $Ta4f_{7/2}$ were also observed. These two peaks were characteristic for Ta_2O_5 and had a spin-orbit splitting of 1.9 eV. Therefore, the nanotubular oxide layer on NT-min and NT-max samples had Ta_2O_5 chemistry. In Fig. 4.5.d and 4.5.e, XPS spectra of NC-min and NC-max are provided. Both of these samples expressed the same 4 peaks observed for NT-min and NT-max. Since the anodization duration for NC-max samples was longer than NC-min, there was a thicker oxide layer on tantalum substrates for the NC-max, and thus Ta_2O_5 peaks for NC-max were more intense compared to NC-min samples in the XPS analysis. In Fig. 4.5.f and 4.5.g, XPS spectra of ND-min and ND-max samples are provided. For the ND-min samples (Fig. 4.5.f), both metallic tantalum (at 21.7 and 23.6 eV) and Ta_2O_5 peaks (29.3 and 26.9 eV) were observed. However, for the ND-max samples (Fig. 4.5.g), in addition to the metallic tantalum peaks at 21.5 and 23.4 eV, non-stoichiometric tantalum oxide (tantalum sub-oxide) peak at 24.8 eV were also detected. This result indicated that during anodization of ND-max samples, an oxide layer having a different stoichiometry than Ta_2O_5 was obtained on sample surfaces. Since ND morphology formed upon the detachment of nanotubular arrays from the tantalum substrates and the bottom surface of the nanotubes had less oxygen anion concentration due to the increased migration depth from the metal/electrolyte surface, oxide layer on ND-max samples did not have enough oxygen to yield Ta_2O_5 stoichiometry [88].

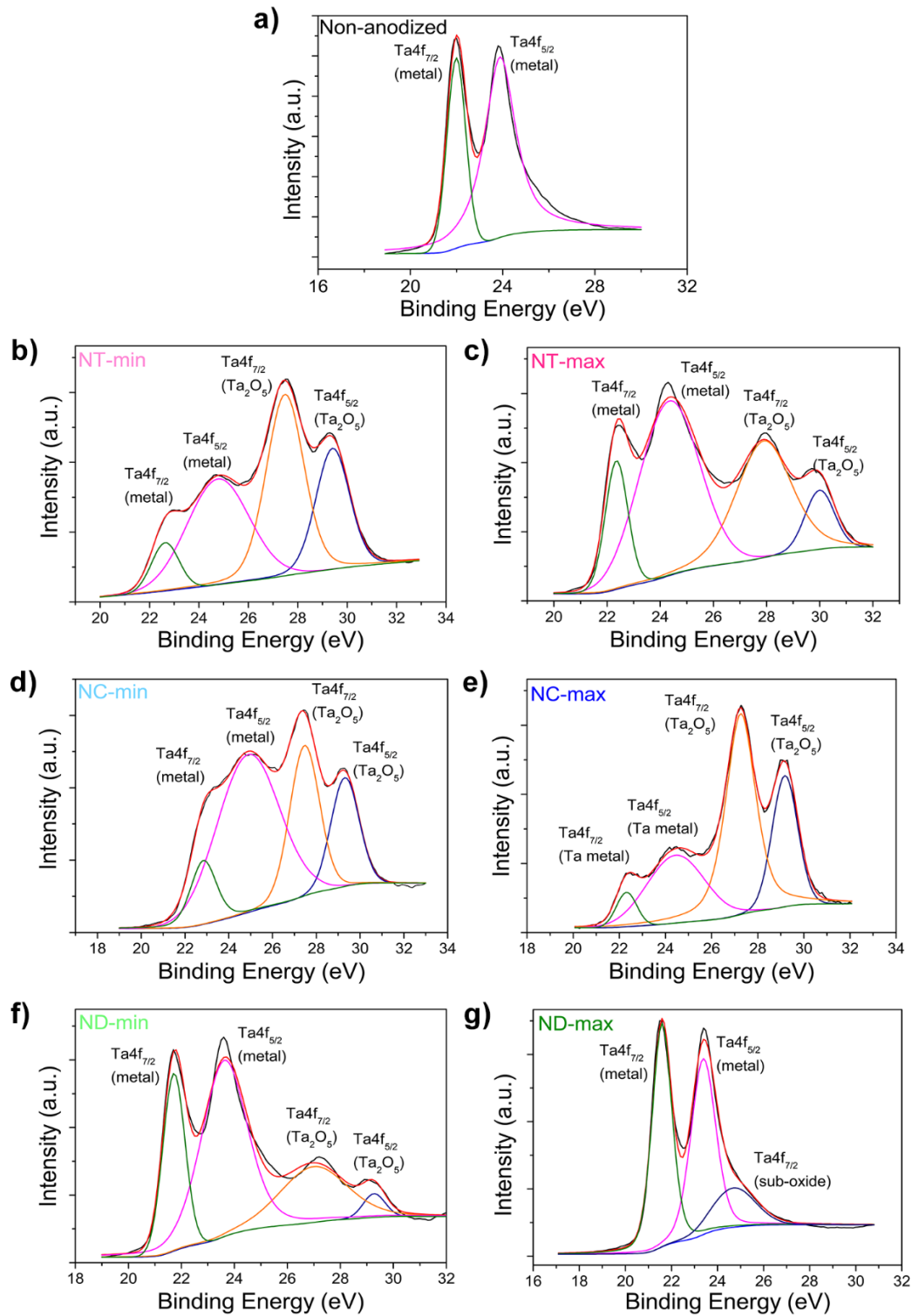


Figure 4.5. High resolution XPS spectra of Ta 4f peaks for a) non-anodized, b) NT-min, c) NT-max, d) NC-min, e) NC-max, f) ND-min and g) ND-max samples.

Sessile drop water contact angles for non-anodized and anodized samples are given in Fig. 4.6. The measured water contact angles were $95^{\circ} \pm 1^{\circ}$, $54^{\circ} \pm 3^{\circ}$, $43^{\circ} \pm 7^{\circ}$, $103^{\circ} \pm 1^{\circ}$, $108^{\circ} \pm 4^{\circ}$, $98^{\circ} \pm 4^{\circ}$ and $93^{\circ} \pm 3^{\circ}$ for non-anodized, NT-min, NT-max, NC-min, NC-max, ND-min and ND-max, respectively. According to these results, NT samples were more hydrophilic compared to non-anodized, NC and ND samples. This was in-line with literature where anodized nanotubular tantalum oxide surfaces exhibited more hydrophilic characteristics compared to their non-anodized counterparts [9]. The reason for hydrophobic nature of NC and ND surfaces can be explained with Cassie Baxter model [71]. During water contact angle measurements of a rough surface, water droplets could not fully spread on the underlying surface due to the entrapment of air molecules within the surface cavities [71]. The entrapped air bubbles inside the nanoporous and nanodimpled surfaces could have led to an increase in the hydrophobicity. For the case of ND samples, DMSO was incorporated inside HF:H₂SO₄ electrolyte during anodization. It could be speculated that in spite of having an oxide-based surface, the incorporated DMSO could also have contributed to the hydrophobic nature of the ND samples.

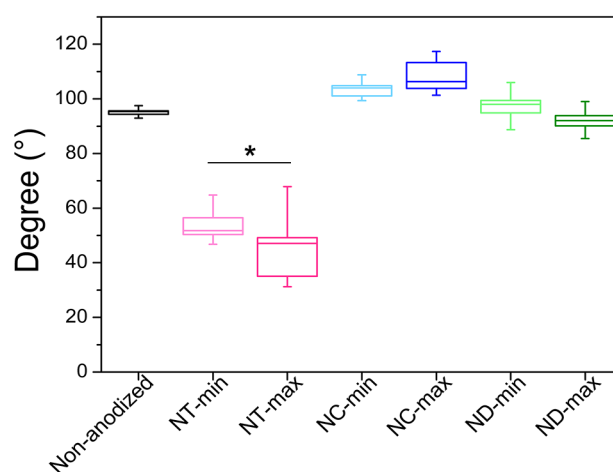
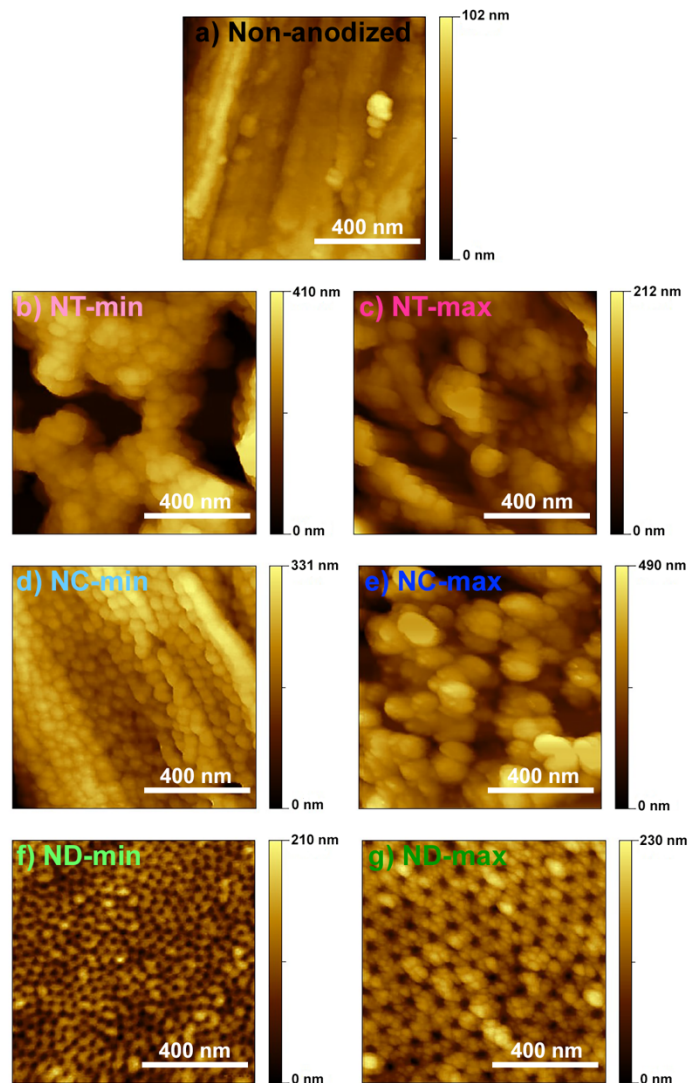


Figure 4.6. Sessile drop water contact angles of non-anodized and anodized tantalum samples. Values are mean \pm SEM, n=3 and *p< 0.05 compared to all other samples.

Atomic force micrographs and nanoroughness measurements of non-anodized and anodized tantalum samples were shown in Fig. 4.7. Nanophase roughness values were measured as 29 ± 2 , 98 ± 3 , 83 ± 3 , 43 ± 2 , 90 ± 4 , 13 ± 2 and 33 ± 4 nm for non-anodized, NT-min, NT-max, NC-min, NC-max, ND-min and ND-max surfaces, respectively (Fig. 4.7.h). Moreover, surface area of the samples were calculated as 1.08 ± 0.09 , 1.82 ± 0.03 , 1.94 ± 0.06 , 1.78 ± 0.04 , 2.23 ± 0.03 , 1.72 ± 0.02 and 2.07 ± 0.03 μm^2 for the non-anodized, NT-min, NT-max, NC-min, NC-max, ND-min and ND-max surfaces, respectively (Fig. 4.7.h). It was clear that nanophase surface roughness of tantalum increased upon anodization for NT and NC samples ($p < 0.01$). However, roughness values for ND samples were similar or even lower than the non-anodized surfaces. The lower nanophase roughness values measured for the ND surface could be attributed to electropolishing of the tantalum samples in 9:1 H_2SO_4 :HF (v/v) + 5 vol% Dimethyl Sulfoxide electrolyte during anodization [89]. As opposed to surface roughness, the surface area of the all anodized samples were higher compared to non-anodized tantalum. It should be noted that the surface roughness measurements and area calculations were limited with the resolution of the AFM tip to interact with nanotubular and nanoporous morphologies on the tantalum surface, and thus surface morphologies of the NT and NC samples could only be partially represented on the AFM micrographs.



h)	Nanophase Roughness, S_q (nm)	Surface Area (μm^2)
Non-anodized	29 ± 2	$1.22 \pm 0.09^*$
NT-min	$84 \pm 3^\#$	1.98 ± 0.03
NT-max	$101 \pm 3^\#$	1.86 ± 0.06
NC-min	$43 \pm 2^\#$	1.78 ± 0.04
NC-max	$90 \pm 4^\#$	2.23 ± 0.03
ND-min	$13 \pm 2^*$	1.72 ± 0.02
ND-max	33 ± 4	2.07 ± 0.03

Figure 4.7. AFM micrographs of a) non-anodized, b) NT-min, c) NT-max, d) NC-min, e) NC-max, f) ND-min and g) ND-max samples. h) Values for the nanophase surface roughness and surface areas of the samples. * $p < 0.01$ compared to all other samples and $^\#p < 0.01$ compared to non-anodized sample. Scale bars are 400 nm.

Results for the total protein adsorption onto anodized and non-anodized tantalum samples are displayed in Fig. 4.8.a. The anodized tantalum samples showed higher protein adsorption compared to the non-anodized tantalum, while no statistical difference was observed between NT-min, NT-max, NC-min, NC-max, ND-min and ND-max samples. It was well documented in the literature that osteoblast proliferation and functions were mediated by the absorbed proteins onto the implant surfaces [39, 40], and the key parameters that control protein adsorption onto implant surfaces include total surface area and surface chemistry [92–94]. In this study, larger surface areas were obtained upon the anodization of tantalum for all investigated surfaces. The increase in surface area of the anodized samples provided more sites for proteins to adsorb and it could provide an explanation for the increased protein adsorption on anodized tantalum surfaces. In addition, XPS analysis revealed that anodization process altered the surface chemistry of tantalum to generate an oxide-based surface layer composed of tantalum sub-oxide and Ta₂O₅. Since proteins tend to adsorb more onto metal oxides than their metal based counter parts [95], altered surface chemistry of the anodized surfaces could contribute to the increased protein adsorption *in vitro*. Surface hydrophobicity did not have a major influence on the total protein adsorption in this study, which was in accord with literature findings [96].

Osteoblast densities on non-anodized and anodized samples (Fig. 4.8.b) did not show any difference between the sample groups at the 1st day of culture ($p > 0.05$). However, at the 3rd day *in vitro*, cellular densities on the NT-min, NT-max, NC-min and ND-max samples were higher compared to the non-anodized tantalum samples, while similar cellular densities were observed on non-anodized, NC-max and ND-min samples. The highest cellular density was observed on ND-max surfaces at the 3rd day of culture ($p < 0.01$). At the 5th day, cell densities on all anodized samples, independent of the surface morphology and the feature size, were higher compared to the non-anodized tantalum samples. Since cells reached confluency at the 5th day *in vitro*, no statistical difference was observed between the osteoblast densities on

anodized tantalum surfaces ($p > 0.05$). We demonstrated that during the anodization, surface chemistry, hydrophobicity, morphology and topography were altered, which led to the observed differences in osteoblast cell densities on non-anodized and anodized surfaces. Specifically, the ND-max samples, despite having hydrophobic characteristics, had the highest cellular density at the 3rd day of culture. The underlying reason for the enhanced osteoblast proliferation on ND-max samples could be explained with its surface area and chemistry. The ND-max samples had nearly twice the surface area of non-anodized samples and non-stoichiometric tantalum oxide (tantalum sub-oxide) chemistry, which was not present in other samples investigated in this study. Since NT-min, NT-max and NC-min samples had similar surface chemistry and surface area, osteoblast proliferation on these samples were similar. On the other hand, the ND-min samples had the lowest nanophase surface roughness and surface area among all anodized tantalum samples, and therefore exhibited the lowest osteoblast density at the 3rd day of culture. However, despite having high surface area and Ta₂O₅ surface chemistry, osteoblast proliferation was also low on NC-max samples *in vitro*. As previously stated, oxide layer delamination was observed at some regions on NC-max surfaces (Supp. Fig. 4.14). It was possible that the detached oxide layer during cellular culture could have some detrimental effects on osteoblast proliferation and led to decreased cellular density compared to other anodized surfaces.

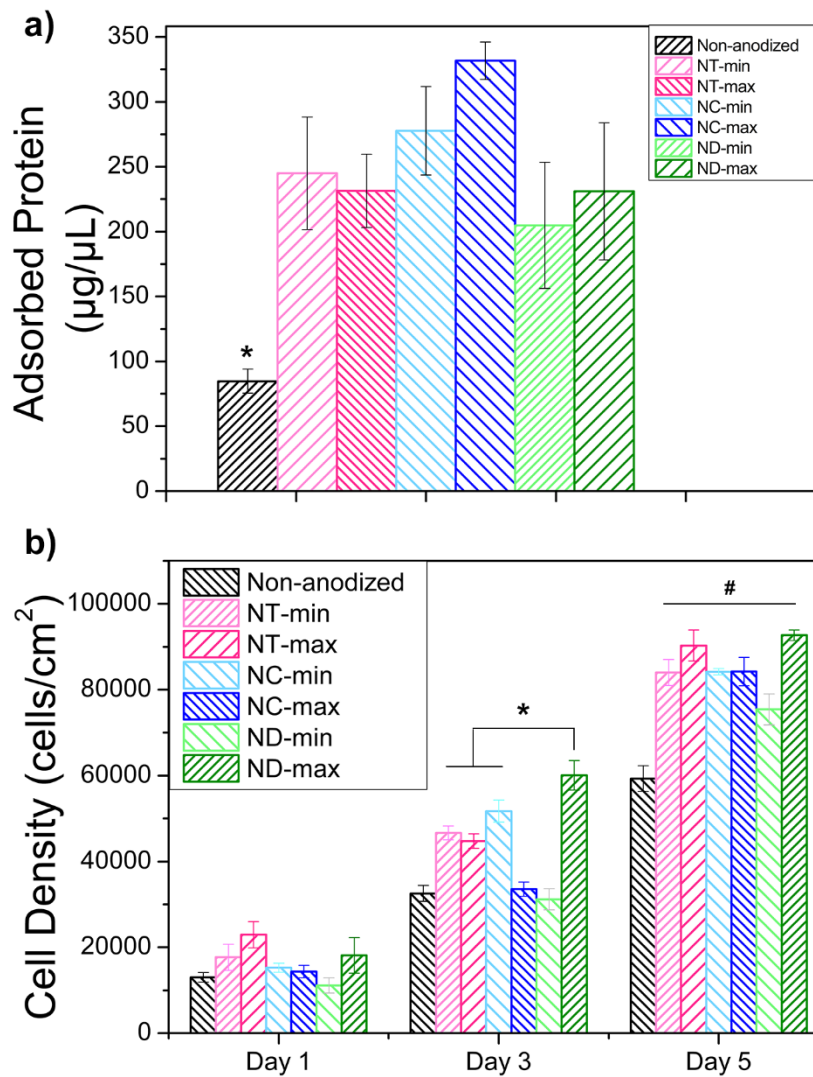


Figure 4.8. a) 4 h protein adsorption and b) 5 day osteoblast proliferation on anodized and non-anodized tantalum samples. Data are mean \pm SEM, $n=3$, * $p < 0.01$ compared to all other samples and # $p < 0.01$ compared to non-anodized tantalum.

In Fig. 4.9, nucleus, f-actin and vinculin stained osteoblasts cultured on non-anodized and anodized samples are displayed. It was clear in these images that osteoblasts adhered and spread on all these samples. Actin filaments were also evident and cellular spreading was measured to be 1.20×10^{-3} , 1.35×10^{-3} , 1.32×10^{-3}

³, 1.36×10^{-3} , 1.23×10^{-3} , 1.39×10^{-3} and 1.47×10^{-3} mm²/cell for non-anodized, NT-min, NT-max, NC-min, NC-max, ND-min and ND-max surfaces, respectively. In addition, the aspect ratio of the cells were calculated to be 1.7, 3.3, 3.5, 3.2, 2.5, 3.5 and 3.6 for non-anodized, NT-min, NT-max, NC-min, NC-max, ND-min and ND-max surfaces, respectively. Quantitative image analysis revealed that the lowest cellular spreading and aspect-ratio was observed on non-anodized samples, while anodization of tantalum improved cellular spreading and aspect-ratio. Vinculin expression levels were calculated to be 9.8, 11.9, 11.5, 10.8, 7.7, 13.2 and 14.8 relative fluorescence intensity/cell for the non-anodized, NT-min, NT-max, NC-min, NC-max, ND-min and ND-max samples, respectively. All the anodized samples, except NC-max, improved vinculin expression. It was interesting to note that osteoblasts cultured on NC-max expressed even lower vinculin levels than the non-anodized samples. The decreased cellular interactions for NC-max samples, which were also shown to have low osteoblast densities in Fig. 8b, could be attributed to the delamination of oxide layer (Supp. Fig. 4.14), as stated previously. Image analysis in fluorescence microscopy also revealed that ND-max samples had the highest aspect ratio, cellular spreading and vinculin expression among all the investigated samples in this study.

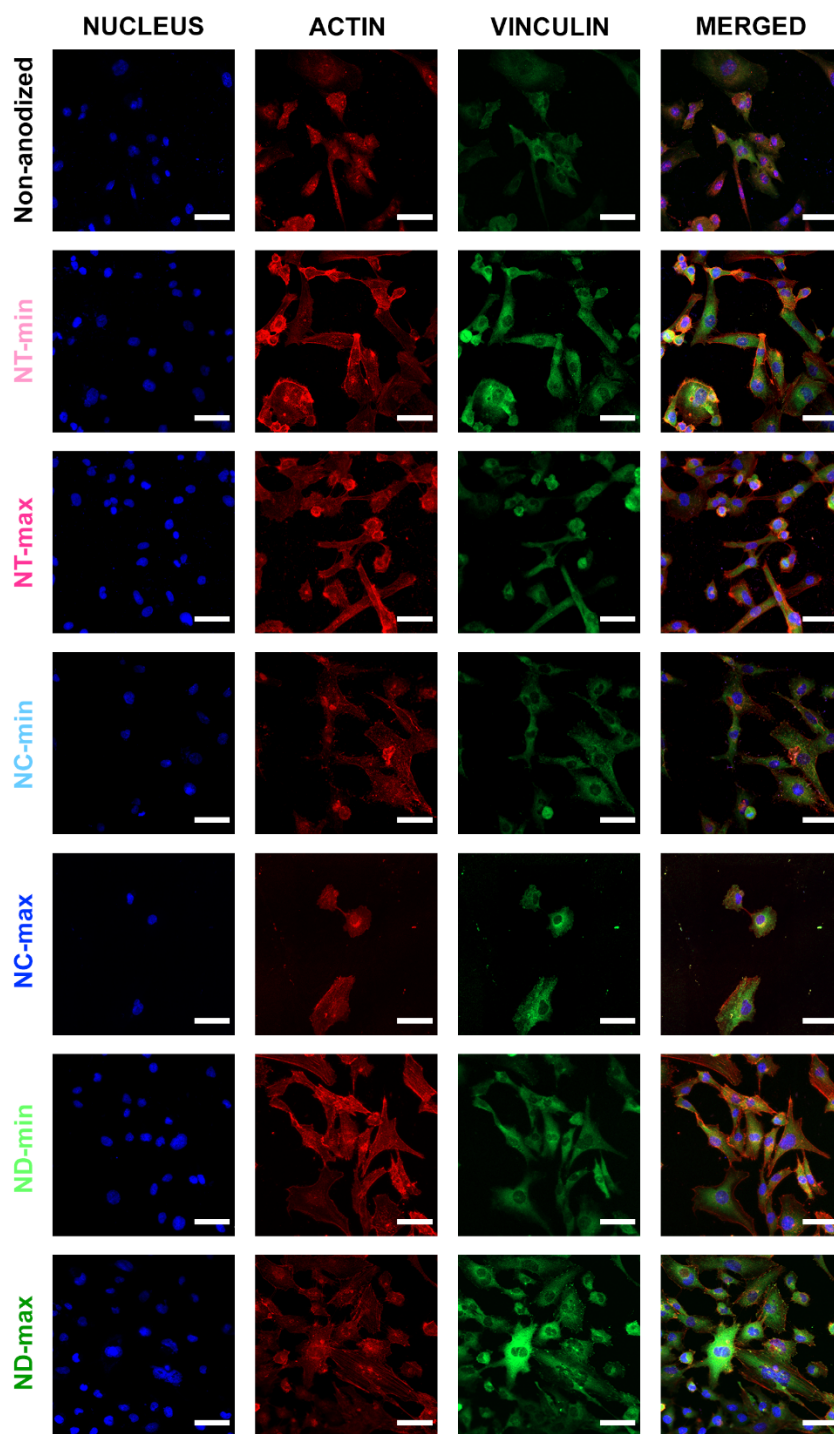


Figure 4.9. Nucleus (blue), actin fiber (red) and vinculin (green) stained osteoblasts at 3rd day of cultured on non-anodized and anodized tantalum samples. The column on the far right shows the merged images. Scale bars are 20 μm .

Osteoblast cellular morphology and cell-surface interactions were further investigated with SEM (Fig. 4.10). Similar to fluorescence microscopy findings, osteoblasts expressed a well-spread morphology on NT-min, NT-max, NC-min, ND-min and ND-max, while circular morphology was evident for osteoblasts cultured on non-anodized surfaces. SEM images of the NC-max samples (Fig.4.10.e) confirmed the presence of broken oxide pieces interacting with osteoblasts and their filipodia. This would further explain the low cellular proliferation, spreading and vinculin expression of osteoblasts upon their interaction with NC-max samples. It was important to note that among all the samples investigated in this study, ND-max samples had the highest osteoblast density and the highest biological interactions.

To conclude, these findings cumulatively point towards the promise of using anodized nanodimpled tantalum oxide surfaces having 90 nm feature size for orthopedic applications.

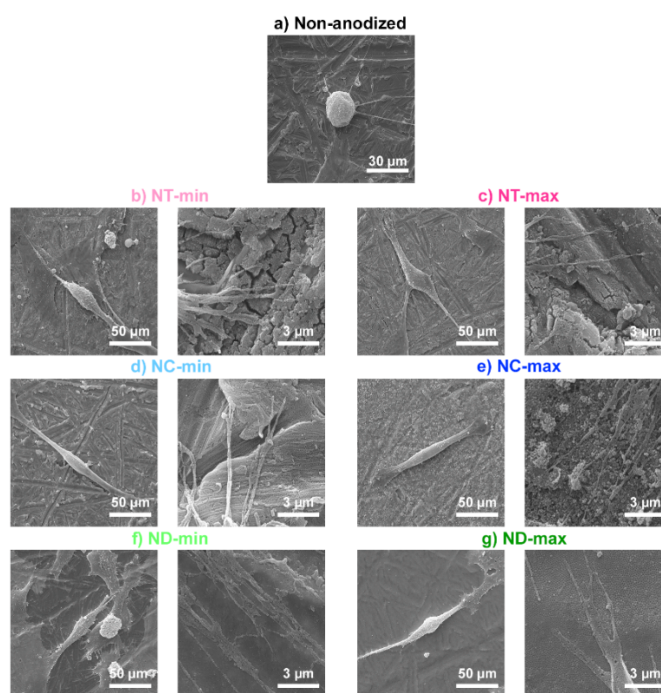


Figure 4.10. SEM micrographs of osteoblasts cultured on non-anodized and anodized tantalum samples at low and high magnification.

4.3 Supporting Information: Controlling the Nanofeature Size and Morphology of Anodized Tantalum Oxide Surfaces for Enhanced Osteoblast Interactions

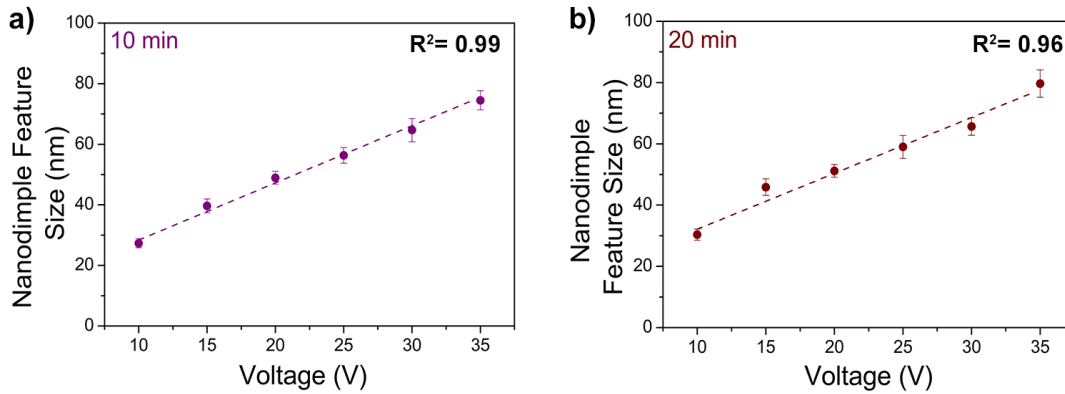


Figure 4.11. Graphs indicate nanodimple feature size vs. voltage for a) 10 min and b) 20 min anodization. Values are mean \pm SEM, n=3.

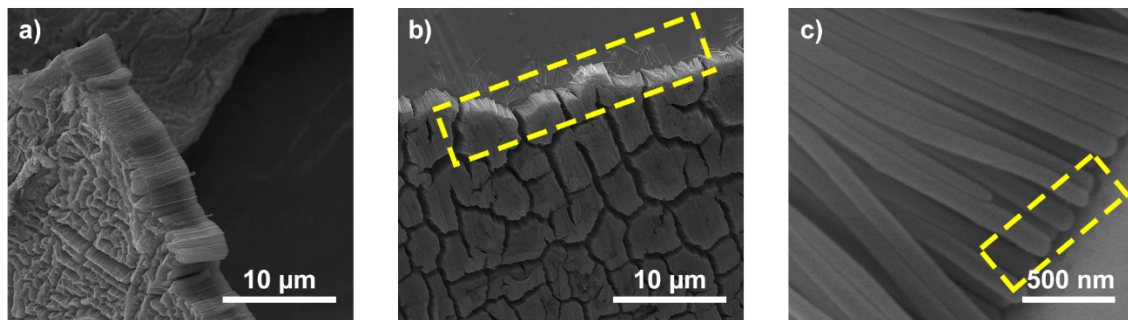


Figure 4.12. a) NT-max samples have free standing nanotubular oxide layer. b) and c) Nanotubular features were not distributed uniformly across the NT-max samples and yellow boxes highlight the regions where delamination occurred.

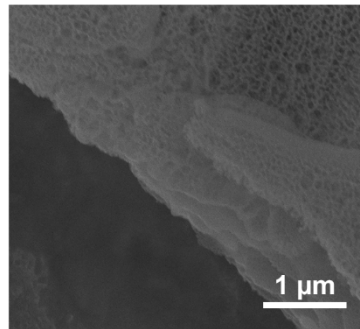


Figure 4.13. Cross-sectional view of an NC sample. Scale bar is 1 μm.

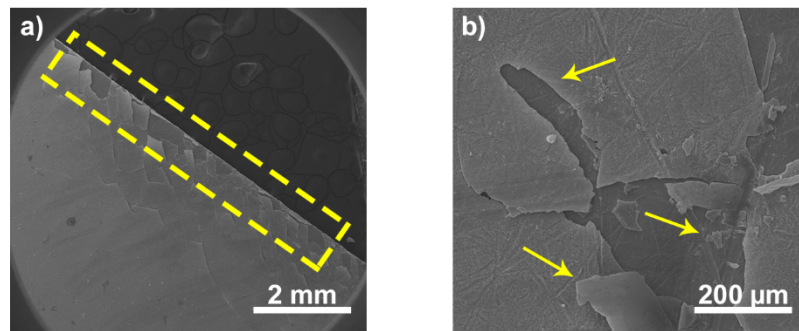


Figure 4.14. Delaminated surface oxide layer of the NC-max samples during cell culture.

CHAPTER 5

CONCLUSION AND FUTURE WORK

In this thesis, anodization was used to modify the surfaces of tantalum to obtain four different feature morphologies, namely nanoporous, nanotubular, nanocoral and nanodimple.

- In the first part of the thesis, tantalum was anodized to improve its biological properties and the findings revealed that nanoporous tantalum oxide surfaces having 25, 35, 45, and 65 nm pore sizes could be fabricated using an aqueous HF:H₂SO₄ solution at 30 V for 5, 10, 15 and 20 min. Surface properties, including chemistry, topography, hydrophilicity and total porosity, could also be altered by anodization depending on the anodization parameters. In addition, this study revealed -for the first time- that fibroblast adhesion and proliferation can be enhanced on anodized nanoporous tantalum oxide samples and fibroblast cells spread more on the anodized surfaces compared to non-porous tantalum. Specifically, anodized surfaces having 25 nm pore size displayed the best biological response due to having a rougher nanophase surface topography, altered surface chemistry and hydrophilic nature of its surfaces. It was concluded that surface modification of tantalum in the nanoscale via anodization could potentially be used to fabricate nanoporous oxide surfaces, which further enhance fibroblast proliferation and cell-surface interaction. This study provided the first evidence for nanoporous tantalum oxide surfaces to be a promising candidate for use in biomaterial applications.
- In the second part of the thesis, oxide based nanofeatures having three distinct morphologies, namely nanotubular, nanocoral and nanodimple, were obtained via anodization on tantalum surfaces. By altering the anodization

parameters, nanofeature sizes were fine-tuned between 20 to 140 nm range, which led to an increase in nanophase roughness and surface area up to 3.5 and 2 folds, respectively. The results also showed that all anodized samples, independent of their surface morphology and feature size, enhanced bone cell proliferation at 5 days *in vitro*. Among the anodized tantalum samples, surfaces having nanodimple morphology with 90 nm feature size showed the highest osteoblast density, cellular spreading and vinculin expression, which was correlated with the presence of tantalum sub-oxide layer and increased surface area of the nanodimpled surfaces. All the obtained results identified anodization to be a potential tool to improve bioactivity of tantalum samples for orthopedic applications.

Apart from these findings, there are some important points that should be considered and investigated for future research.

- Although promising results were obtained for anodized tantalum surfaces compared to non-anodized tantalum, delamination of oxide films is still a major problem, especially for nanocoral surfaces. Since implantation process involves application of mechanical load onto nanofeatured surfaces, good adhesion strength between oxide films and the substrate should be provided. Without finding a potential solution for delamination of nanocoral surfaces, animal experiments and clinical trials for that surfaces are not possible. Therefore, it is necessary to address this problem by interacting non-protonated polar substances, *i.e.* cyclohexane to enhance adhesion strength of the nanocoral surfaces onto tantalum substrate [97].
- In spite of having remarkable properties for orthopedic applications, high density of tantalum is still a problem, preventing development of implant. As a remedy, tantalum foams will be fabricated and further anodized to enhance its biological properties. In addition, elastic modulus of tantalum foams is nearly 3 GPa which is similar to that of trabecular bone [98]. This will also prevent stress-shielding and increase longevity of the implant.

- In this thesis, potential of anodized tantalum surfaces having feature sizes between 20-140 nm for orthopedic applications was examined successfully *in vitro*. However, as a next step, this research should be enlarged *in vitro* by examining other biological tests, *i.e.* vascular growth, osteoclast functions, immune cell response and antibacterial properties. Most importantly, it should be followed by *in vivo* large animal tests. By doing so, researchers can understand both advantages and disadvantages of anodized tantalum surfaces and this research can be translated potentially to clinical use.

REFERENCES

- [1] S. Minagar, C. C. Berndt, J. Wang, E. Ivanova, and C. Wen, “A review of the application of anodization for the fabrication of nanotubes on metal implant surfaces,” *Acta Biomaterialia*, vol. 8, no. 8, pp. 2875–2888, Aug-2012.
- [2] D. A. Florea, D. Albuț, A. M. Grumezescu, and E. Andronescu, “Surface modification – A step forward to overcome the current challenges in orthopedic industry and to obtain an improved osseointegration and antimicrobial properties,” *Materials Chemistry and Physics*, vol. 243, no. August 2019, p. 122579, 2020.
- [3] V. Sansone, D. Pagani, and M. Melato, “The effects on bone cells of metal ions released from orthopaedic implants. A review,” *Clinical Cases in Mineral and Bone Metabolism*, vol. 10, no. 1, pp. 34–40, 2013.
- [4] E. Losina *et al.*, “Lifetime medical costs of knee osteoarthritis management in the US,” vol. 67, no. 2, pp. 203–215, 2016.
- [5] W. Chen *et al.*, “Study on morphology evolution of anodic tantalum oxide films in different using stages of H₂SO₄/HF electrolyte,” *Electrochimica Acta*, vol. 236, pp. 140–153, May 2017.
- [6] Y. J. Zeng *et al.*, “Enhanced biocompatibility in anodic TaO_x nanotube arrays,” *Nanoscale Research Letters*, vol. 12, no. 557, pp. 1–8, 2017.
- [7] G. Balasundaram and T. J. Webster, “A perspective on nanophase materials for orthopedic implant applications,” *Journal of Materials Chemistry*, vol. 16, no. 38, pp. 3737–3745, 2006

- [8] M. Stiehler *et al.*, “Morphology, proliferation, and osteogenic differentiation of mesenchymal stem cells cultured on titanium, tantalum, and chromium surfaces,” *Journal of Biomedical Materials Research - Part A*, vol. 86, no. 2, pp. 448–458, Aug. 2008.
- [9] N. Wang, H. Li, J. Wang, S. Chen, Y. Ma, and Z. Zhang, “Study on the anticorrosion, biocompatibility, and osteoinductivity of tantalum decorated with tantalum oxide nanotube array films,” *ACS Applied Materials and Interfaces*, vol. 4, no. 9, pp. 4516–4523, Sep. 2012.
- [10] T. V. Molchan, G. E. Thompson, P. Skeldon, X. Zhong, and I. S. Molchan, “The effect of post-anodizing rinsing on the morphology and composition of porous and nanotubular anodic films generated on titanium,” *Electrochimica Acta*, vol. 176, pp. 1233–1238, Aug. 2015.
- [11] W. Lee and S. J. Park, “Porous anodic aluminum oxide: Anodization and templated synthesis of functional nanostructures,” *Chemical Reviews*, vol. 114, no. 15, pp. 7487–7556, 2014.
- [12] B. E. Schwartz, H. I. Piponov, C. W. Helder, W. F. Mayers, and M. H. Gonzalez, “Revision total hip arthroplasty in the United States: national trends and in-hospital outcomes,” *International Orthopaedics*, vol. 40, no. 9, pp. 1793–1802, 2016.
- [13] Total Knee Replacement. Retrieved March 25, 2018 from <https://www.thecenteroregon.com/total-knee-replacement/>.
- [14] L. Zhang and T. J. Webster, “Nanotechnology and nanomaterials: Promises for improved tissue regeneration,” *Nano Today*, vol. 4, no. 1, pp. 66–80, 2009.

- [15] V. P. Mantripragada, B. Lecka-Czernik, N. A. Ebraheim, and A. C. Jayasuriya, "An overview of recent advances in designing orthopedic and craniofacial implants," *Journal of Biomedical Materials Research Part A*, vol. 101, no. 11, p. NA-NA, Jun. 2012.
- [16] R. Petersen, "Titanium implant osseointegration problems with alternate solutions using epoxy/carbon-fiber-reinforced composite," *Metals*, vol. 4, no. 4, pp. 549–569, Dec. 2014.
- [17] S. Parithimarkalaignan and T. V. Padmanabhan, "Osseointegration: An update," *Journal of Indian Prosthodontist Society*, vol. 13, no. 1, pp. 2–6, 2013.
- [18] J. Walczak, F. Shahgaldi, and F. Heatley, "In vivo corrosion of 316L stainless-steel hip implants: morphology and elemental compositions of corrosion products," *Biomaterials*, vol. 19, pp. 229-237, 1998.
- [19] L. N. Wang, M. Jin, Y. Zheng, Y. Guan, X. Lu, and J. L. Luo, "Nanotubular surface modification of metallic implants via electrochemical anodization technique," *International Journal of Nanomedicine*, vol. 9, pp. 4421–4435, 2014.
- [20] M. Z. Ibrahim, A. A. D. Sarhan, F. Yusuf, and M. Hamdi, "Biomedical materials and techniques to improve the tribological, mechanical and biomedical properties of orthopedic implants – A review article," *Journal of Alloys and Compounds*, vol. 714, no. April, pp. 636–667, 2017.
- [21] S. Minagar, C. C. Berndt, J. Wang, E. Ivanova, and C. Wen, "A review of the application of anodization for the fabrication of nanotubes on metal implant surfaces," *Acta Biomaterialia*, vol. 8, no. 8, pp. 2875–2888, 2012.

- [22] N. Patil, K. Lee, and S. B. Goodman, "Porous tantalum in hip and knee reconstructive surgery," *Journal of Biomedical Materials Research - Part B Applied Biomaterials*, vol. 89, no. 1. John Wiley and Sons Inc., pp. 242–251, 2009.
- [23] N. C. Stephenson and R. S. Roth, "Structural systematics in the binary system Ta₂O₅–WO₃. V. The structure of the low-temperature form of tantalum oxide L-Ta₂O₅," *Acta Crystallographica Section B Structural Crystallography and Crystal Chemistry*, vol. 27, no. 5, pp. 1037–1044, 1971.
- [24] J. Ma, Y. Sun, R. Zan, J. Ni, and X. Zhang, "Cellular different responses to different nanotube inner diameter on surface of pure tantalum," *Materials Science and Engineering C*, vol. 109, no. December 2019, 2020.
- [25] G. Xu, X. Shen, Y. Hu, P. Ma, and K. Cai, "Fabrication of tantalum oxide layers onto titanium substrates for improved corrosion resistance and cytocompatibility," *Surface and Coatings Technology*, vol. 272, pp. 58–65, 2015.
- [26] L. Fialho and S. Carvalho, "Surface engineering of nanostructured Ta surface with incorporation of osteoconductive elements by anodization," *Applied Surface Science*, vol. 495, no. May, p. 143573, 2019.
- [27] Y. Liu, C. Bao, D. Wismeijer, and G. Wu, "The physicochemical/biological properties of porous tantalum and the potential surface modification techniques to improve its clinical application in dental implantology," *Materials Science and Engineering C*, vol. 49. Elsevier Ltd, pp. 323–329, 01-Apr-2015.

- [28] R. Pillar, "Metallic Biomaterials," in *Biomedical Materials*, 1st ed., Wiley, 2009, p. 49.
- [29] A. Biesiekierski, J. Wang, M. Abdel-Hady Gepreel, and C. Wen, "A new look at biomedical Ti-based shape memory alloys," *Acta Biomaterialia*, vol. 8, no. 5, pp. 1661–1669, 2012.
- [30] X. Wang *et al.*, "Topological design and additive manufacturing of porous metals for bone scaffolds and orthopaedic implants: A review," *Biomaterials*, vol. 83, pp. 127–141, 2016.
- [31] S. Kumar, M. Nehra, D. Kedia, N. Dilbaghi, K. Tankeshwar, and K. H. Kim, "Nanotechnology-based biomaterials for orthopaedic applications: Recent advances and future prospects," *Materials Science and Engineering C*, vol. 106, no. September 2019, p. 110154, 2020.
- [32] I. Firkowska-Boden, X. Zhang, and K. D. Jandt, "Controlling protein adsorption through nanostructured polymeric surfaces," *Advanced Healthcare Materials*, vol. 7, no. 1, 2018.
- [33] D. Ganguly, R. Shahbazian-Yassar, and T. Shokuhfar, "Recent advances in nanotubes for orthopedic implants," *Journal of Nanotechnology and Smart Materials*, vol.1, no. 201, pp. 1-10, 2014.
- [34] R. An *et al.*, "Nanolamellar tantalum interfaces in the osteoblast adhesion," *Langmuir*, vol. 35, no. 7, pp. 2480–2489, 2019.
- [35] W. T. Huo, L. Z. Zhao, S. Yu, Z. T. Yu, P. X. Zhang, and Y. S. Zhang, "Significantly enhanced osteoblast response to nano-grained pure tantalum," *Scientific Reports*, vol. 7, pp. 1–13, 2017.

- [36] C. Hu, D. Ashok, D. R. Nisbet, and V. Gautam, "Bioinspired surface modification of orthopedic implants for bone tissue engineering," *Biomaterials*, vol. 219, no. February, p. 119366, 2019.
- [37] M. M. Momeni, M. Mirhosseini, M. Chavoshi, and A. Hakimizade, "The effect of anodizing voltage on morphology and photocatalytic activity of tantalum oxide nanostructure," *Journal of Materials Science: Materials in Electronics*, vol. 27, no. 4, pp. 3941–3947, Apr. 2016.
- [38] H. A. El-Sayed, C. A. Horwood, A. D. Abhayawardhana, and V. I. Birss, "New insights into the initial stages of Ta oxide nanotube formation on polycrystalline Ta electrodes," *Nanoscale*, vol. 5, no. 4, pp. 1494–1498, Feb. 2013.
- [39] H. A. El-Sayed and V. I. Birss, "Controlled growth and monitoring of tantalum oxide nanostructures," *Nanoscale*, vol. 2, no. 5, pp. 793–798, 2010.
- [40] C. A. Horwood, H. A. El-Sayed, and V. I. Birss, "Precise electrochemical prediction of short tantalum oxide nanotube length," *Electrochimica Acta*, vol. 132, pp. 91–97, Jun. 2014.
- [41] A. El Ruby Mohamed and S. Rohani, "Modified TiO₂ nanotube arrays (TNTAs): Progressive strategies towards visible light responsive photoanode, a review," *Energy and Environmental Science*, vol. 4, no. 4, pp. 1065–1086, 2011.
- [42] S. Minagar, C. Berndt, and C. Wen, "Fabrication and characterization of nanoporous niobia, and nanotubular tantalum, titania and zirconia via anodization," *Journal of Functional Biomaterials*, vol. 6, no. 2, pp. 153–170, Mar. 2015.

- [43] I. Sieber, B. Kannan, and P. Schmuki, "Self-assembled porous tantalum oxide prepared in H₂SO₄/HF electrolytes," *Electrochemical and Solid-State Letters*, vol. 8, no. 3, p. J10, 2005.
- [44] W. Wei, J. M. Macak, N. K. Shrestha, and P. Schmuki, "Thick self-ordered nanoporous Ta₂O₅ films with long-range lateral order," *Journal of The Electrochemical Society*, vol. 156, no. 6, p. K104, Apr. 2009.
- [45] C. Yao, E. B. Slamovich, and T. J. Webster, "Enhanced osteoblast functions on anodized titanium with nanotube-like structures," *Journal of Biomedical Materials Research - Part A*, vol. 85, no. 1, pp. 157–166, 2008.
- [46] K. Huo, B. Gao, J. Fu, L. Zhao, and P. K. Chu, "Fabrication, modification, and biomedical applications of anodized TiO₂ nanotube arrays," *RSC Advances*, vol. 4, no. 33, pp. 17300–17324, 2014.
- [47] Z. X. Chen, Y. Takao, W. X. Wang, T. Matsubara, and L. M. Ren, "Surface characteristics and in vitro biocompatibility of titanium anodized in a phosphoric acid solution at different voltages," *Biomedical Materials*, vol. 4, no. 6, 2009.
- [48] S. Altuntas, F. Buyukserin, A. Haider, B. Altinok, N. Biyikli, and B. Aslim, "Protein-releasing conductive anodized alumina membranes for nerve-interface materials," *Materials Science and Engineering C*, vol. 67, pp. 590–598, 2016.
- [49] G. Sriram *et al.*, "Current trends in nanoporous anodized alumina platforms for biosensing applications," *Journal of Nanomaterials*, vol. 2016, pp. 1-24, 2016.

- [50] C. Toccafondi and S. Thorat, "Multifunctional substrates of thin porous alumina for cell biosensors," pp. 2411–2420, 2014.
- [51] A. El Merhie, M. Salerno, C. Toccafondi, and S. Dante, "Neuronal-like response of N2a living cells to nanoporous patterns of thin supported anodic alumina," *Colloids and Surfaces B: Biointerfaces*, vol. 178, no. January, pp. 32–37, 2019.
- [52] M. Salerno, F. Caneva-Soumetz, L. Pastorino, N. Patra, A. Diaspro, and C. Ruggiero, "Adhesion and proliferation of osteoblast-like cells on anodic porous alumina substrates with different morphology," *IEEE Transactions on Nanobioscience*, vol. 12, no. 2, pp. 106–111, 2013.
- [53] F. S. Tabatabaei and M. Torshabi, "In vitro proliferation and osteogenic differentiation of endometrial stem cells and dental pulp stem cells," *Cell and Tissue Banking*, vol. 18, no. 2, pp. 239–247, 2017.
- [54] K. C. Popat *et al.*, "Influence of nanoporous alumina membranes on long-term osteoblast response," *Biomaterials*, vol. 26, no. 22, pp. 4516–4522, 2005.
- [55] M. Qadir, J. Lin, A. Biesiekierski, Y. Li, and C. Wen, "Effect of anodized TiO₂-Nb₂O₅-ZrO₂ nanotubes with different nanoscale dimensions on the biocompatibility of a Ti₃₅Zr₂₈Nb alloy," *ACS Applied Materials and Interfaces*, 2020.
- [56] N. K. Awad, S. L. Edwards, and Y. S. Morsi, "A review of TiO₂ NTs on Ti metal: Electrochemical synthesis, functionalization and potential use as bone implants," *Materials Science and Engineering C*, vol. 76, pp. 1401–1412, 2017.

- [57] C. Von Wilmsowsky, S. Bauer, S. Roedl, F. W. Neukam, P. Schmuki, and K. A. Schlegel, "The diameter of anodic TiO₂ nanotubes affects bone formation and correlates with the bone morphogenetic protein-2 expression in vivo," *Clinical Oral Implants Research*, vol. 23, no. 3, pp. 359–366, 2012.
- [58] T. Ruckh, J. R. Porter, N. K. Allam, X. Feng, C. A. Grimes, and K. C. Popat, "Nanostructured tantalum as a template for enhanced osseointegration," *Nanotechnology*, vol. 20, no. 4, pp. 1-7, 2009.
- [59] E. Uslu, H. Öztatlı, B. Garipcan, and B. Ercan, "Fabrication and cellular interactions of nanoporous tantalum oxide," *Journal of Biomedical Materials Research - Part B Applied Biomaterials*, no. January, pp. 1–11, 2020.
- [60] K. Von Der Mark, S. Bauer, J. Park, and P. Schmuki, "Another look at 'Stem cell fate dictated solely by altered nanotube dimension,'" *Proceedings of the National Academy of Sciences of the United States of America*, vol. 106, no. 24, 2009.
- [61] H. Yu, S. Zhu, X. Yang, X. Wang, H. Sun, and M. Huo, "Synthesis of coral-like tantalum oxide films via anodization in mixed organic-inorganic electrolytes," *PLoS ONE*, vol. 8, no. 6, 2013.
- [62] M. Thommes *et al.*, "Physisorption of gases, with special reference to the evaluation of surface area and pore size distribution (IUPAC Technical Report)," *Pure and Applied Chemistry*, vol. 87, no. 9–10, pp. 1051–1069, 2015.
- [63] R. Simpson, R. G. White, J. F. Watts, and M. A. Baker, "XPS investigation of monatomic and cluster argon ion sputtering of tantalum pentoxide," *Applied Surface Science*, vol. 405, pp. 79–87, 2017.

- [64] T. M. Pan, Y. S. Huang, and J. L. Her, "Sensing and impedance characteristics of YbTaO₄ sensing membranes," *Scientific Reports*, vol. 8, no. 1, pp. 1–11, 2018.
- [65] T. Lertvanithphol *et al.*, "Spectroscopic study on amorphous tantalum oxynitride thin films prepared by reactive gas-timing RF magnetron sputtering," *Applied Surface Science*, vol. 492, no. February, pp. 99–107, 2019.
- [66] P. K. Srivas, K. Kapat, B. Das, P. Pal, P. G. Ray, and S. Dhara, "Hierarchical surface morphology on Ti6Al4V via patterning and hydrothermal treatment towards improving cellular response," *Applied Surface Science*, vol. 478, no. February, pp. 806–817, 2019.
- [67] M. Kulkarni *et al.*, "Protein interactions with layers of TiO₂ nanotube and nanopore arrays: Morphology and surface charge influence," *Acta Biomaterialia*, vol. 45, pp. 357–366, 2016.
- [68] F. A. Bruera, G. R. Kramer, M. L. Vera, and A. E. Ares, "Synthesis and morphological characterization of nanoporous aluminum oxide films by using a single anodization step," *Coatings*, vol. 9, no. 2, 2019.
- [69] A. Gao, R. Hang, L. Bai, B. Tang, and P. K. Chu, "Electrochemical surface engineering of titanium-based alloys for biomedical application," *Electrochimica Acta*, vol. 271, pp. 699–718, 2018.
- [70] K. Kim, B. A. Lee, X. H. Piao, H. J. Chung, and Y. J. Kim, "Surface characteristics and bioactivity of an anodized titanium surface," *Journal of Periodontal and Implant Science*, vol. 43, no. 4, pp. 198–205, 2013.

- [71] T. Koishi, K. Yasuoka, S. Fujikawa, T. Ebisuzaki, and C. Z. Xiao, “Coexistence and transition between Cassie and Wenzel state on pillared hydrophobic surface,” *Proceedings of the National Academy of Sciences of the United States of America*, vol. 106, no. 21, pp. 8435–8440, 2009.
- [72] S. Kim, A. A. Polycarpou, and H. Liang, “Electrical-potential induced surface wettability of porous metallic nanostructures,” *Applied Surface Science*, vol. 351, pp. 460–465, 2015.
- [73] K. Shankar *et al.*, “Highly-ordered TiO₂ nanotube arrays up to 220 μm in length: Use in water photoelectrolysis and dye-sensitized solar cells,” *Nanotechnology*, vol. 18, no. 6, pp. 1-11, 2007.
- [74] C. E. Tanase, M. Golozar, S. M. Best, and R. A. Brooks, “Cell response to plasma electrolytic oxidation surface-modified low-modulus β -type titanium alloys,” *Colloids and Surfaces B: Biointerfaces*, vol. 176, no. July 2018, pp. 176–184, 2019.
- [75] M. B. Hovgaard, K. Rechendorff, J. Chevallier, M. Foss, and F. Besenbacher, “Fibronectin adsorption on tantalum: The influence of nanoroughness,” *Journal of Physical Chemistry B*, vol. 112, no. 28, pp. 8241–8249, Jul. 2008.
- [76] E. Rosqvist *et al.*, “Human dermal fibroblast proliferation controlled by surface roughness of two-component nanostructured latex polymer coatings,” *Colloids and Surfaces B: Biointerfaces*, vol. 174, no. October 2018, pp. 136–144, 2019.

- [77] K. Webb, V. Hlady, and P. A. Tresco, "Relative importance of surface wettability and charged functional groups on NIH 3T3 fibroblast attachment, spreading, and cytoskeletal organization," *Journal of Biomedical Materials Research*, vol. 41, no. 3, pp. 422–430, 1998.
- [78] K. Indira, U. K. Mudali, T. Nishimura, and N. Rajendran, "A review on TiO₂ nanotubes: Influence of anodization parameters, formation mechanism, properties, corrosion behavior, and biomedical Applications," *Journal of Bio- and Tribo-Corrosion*, vol. 1, no. 4, pp. 1–22, 2015.
- [79] Y. J. Park, J. M. Ha, G. Ali, H. J. Kim, Y. Addad, and S. O. Cho, "Controlled fabrication of nanoporous oxide layers on zircaloy by anodization," *Nanoscale Research Letters*, vol. 10, no. 1, pp. 28–31, 2015.
- [80] S. Grigorescu, S. So, J. E. Yoo, A. Mazare, R. Hahn, and P. Schmuki, "Open top anodic Ta₃N₅ nanotubes for higher solar water splitting efficiency," *Electrochimica Acta*, vol. 182, pp. 803–808, Nov. 2015.
- [81] P. Roy, S. Berger, and P. Schmuki, "TiO₂ nanotubes: Synthesis and applications," *Angewandte Chemie - International Edition*, vol. 50, no. 13, pp. 2904–2939, 2011.
- [82] V. Parkhutik, J. Curiel-Esparza, M. C. Millan, and J. Albella, "Spontaneous layering of porous silicon layers formed at high current densities," *Physica Status Solidi (A) Applications and Materials Science*, vol. 202, no. 8, pp. 1576–1580, 2005.
- [83] L. Fialho, C. F. Almeida Alves, L. S. Marques, and S. Carvalho, "Development of stacked porous tantalum oxide layers by anodization," *Applied Surface Science*, vol. 511, no. January, p. 145542, 2020.

- [84] H. A. El-Sayed and V. I. Birss, "Controlled interconversion of nanoarray of Ta dimples and high aspect ratio Ta oxide nanotubes," *Nano Letters*, vol. 9, no. 4, pp. 1350–1355, Apr. 2009.
- [85] X. Feng, T. J. LaTempa, J. I. Bastiam, G. K. Mor, O. K. Varghese, and C. A. Grimes, "Ta₃N₅ nanotube arrays for visible light water photoelectrolysis," *Nano Letters*, vol. 10, no. 3, pp. 948–952, Mar. 2010.
- [86] M. Khanuja, H. Sharma, B. R. Mehta, and S. M. Shivaprasad, "XPS depth-profile of the suboxide distribution at the native oxide/Ta interface," *Journal of Electron Spectroscopy and Related Phenomena*, vol. 169, no. 1, pp. 41–45, 2009.
- [87] I. Perez, V. Sosa, F. G. Perera, J. T. Elizalde Galindo, J. L. Enríquez-Carrejo, and P. G. Mani González, "Effect of ion bombardment on the chemical properties of crystalline tantalum pentoxide films," *Vacuum*, vol. 165, no. April, pp. 274–282, 2019.
- [88] Piszczek *et al.*, "Comprehensive evaluation of the biological properties of surface-modified titanium alloy implants," *Journal of Clinical Medicine*, vol. 9, no. 2, p. 342, 2020.
- [89] H. El-Sayed, S. Singh, M. T. Greiner, and P. Kruse, "Formation of highly ordered arrays of dimples on tantalum at the nanoscale," *Nano Letters*, vol. 6, no. 12, pp. 2995–2999, Dec. 2006.
- [90] M. Hindié, M. C. Degat, F. Gaudire, O. Gallet, P. R. Van Tassel, and E. Pauthe, "Pre-osteoblasts on poly(l-lactic acid) and silicon oxide: Influence of fibronectin and albumin adsorption," *Acta Biomaterialia*, vol. 7, no. 1, pp. 387–394, 2011.

- [91] D. E. MacDonald, B. E. Rapuano, N. Deo, M. Stranick, P. Somasundaran, and A. L. Boskey, "Thermal and chemical modification of titanium-aluminum-vanadium implant materials: Effects on surface properties, glycoprotein adsorption, and MG63 cell attachment," *Biomaterials*, vol. 25, no. 16, pp. 3135–3146, 2004.
- [92] R. Jimbo, M. Ivarsson, A. Koskela, Y.-T. Sul, and C. B. Johansson, "Protein adsorption to surface chemistry and crystal structure modification of titanium surfaces," *Journal of Oral and Maxillofacial Research*, vol. 1, no. 3, pp. 1–9, 2010.
- [93] B. Sivaraman, K. P. Fears, and R. A. Latour, "Investigation of the effects of surface chemistry and solution concentration on the conformation of adsorbed proteins using an improved circular dichroism method," *Langmuir*, vol. 25, no. 5, pp. 3050–3056, 2009.
- [94] P. Rico, J. C. R. Hernández, D. Moratal, G. Altankov, M. M. Pradas, and M. Salmerón-Sánchez, "Substrate-induced assembly of fibronectin into networks: Influence of surface chemistry and effect on osteoblast adhesion," *Tissue Engineering - Part A*, vol. 15, no. 11, pp. 3271–3281, 2009.
- [95] M. Talha, Y. Ma, P. Kumar, Y. Lin, and A. Singh, "Role of protein adsorption in the bio corrosion of metallic implants – A review," *Colloids and Surfaces B: Biointerfaces*, vol. 176, no. February, pp. 494–506, 2019.
- [96] C. F. Wertz and M. M. Santore, "Effect of surface hydrophobicity on adsorption and relaxation kinetics of albumin and fibrinogen : single-species and competitive behavior," no. 25, pp. 3006–3016, 2001.

- [97] M. Zhao *et al.*, “Gradient control of the adhesive force between Ti/TiO₂ nanotubular arrays fabricated by anodization,” *Scientific Reports*, vol. 4, pp. 1–7, 2014.
- [98] P. Sevilla, C. Aparicio, J. A. Planell, and F. J. Gil, “Comparison of the mechanical properties between tantalum and nickel-titanium foams implant materials for bone ingrowth applications,” *Journal of Alloys and Compounds*, vol. 439, no. 1–2, pp. 67–73, 2007.